Jones, T. J., McNamara, K., Eychenne, J., Rust, A. C., Cashman, K. V., Scheu, B., & Edwards, R. (2016). Primary and secondary fragmentation of crystal-bearing intermediate magma. *Journal of Volcanology and Geothermal Research*, *327*, 70-83. https://doi.org/10.1016/j.jvolgeores.2016.06.022

Elsevier Editorial System(tm) for Journal of Volcanology and Geothermal Research
Manuscript Draft

Manuscript Number: VOLGEO5083R1

Title: Primary and secondary fragmentation of crystal-bearing intermediate magma

Article Type: Research paper

Keywords: Volcanic ash; Fragmentation; Broken crystals; Milling; Fractals; X-ray computed tomography

Corresponding Author: Mr. Thomas James Jones,

Corresponding Author's Institution: Durham University

First Author: Thomas James Jones

Order of Authors: Thomas James Jones; Keri McNamara; Julia Eychenne; Alison C Rust; Katharine V Cashman; Bettina Scheu; Robyn Edwards

Abstract: Crystal-rich intermediate magmas are subjected to both primary and secondary fragmentation processes, each of which may produce texturally distinct tephra. Of particular interest for volcanic hazards is the extent to which each process contributes ash to volcanic plumes. One way to address this question is by fragmenting pyroclasts under controlled conditions. We fragmented pumice samples from Soufriere Hills Volcano (SHV), Montserrat, by three methods: rapid decompression in a shock tube-like apparatus, impact by a falling piston, and milling in a ball mill. Grain size distributions of the products reveal that all three mechanisms produce fractal breakage patterns, and that the fractal dimension increases from a minimum of ~2.1 for decompression fragmentation (primary fragmentation) to a maximum of ~ 2.7 by repeated impact (secondary fragmentation). To assess the details of the fragmentation process, we quantified the shape, texture and components of constituent ash particles. Ash shape analysis shows that the axial ratio increases during milling and that particle convexity increases with repeated impacts. We also quantify the extent to which the matrix is separated from the crystals, which shows that secondary processes efficiently remove adhering matrix from crystals, particularly during milling (abrasion). Furthermore, measurements of crystal size distributions before (using x-ray computed tomography) and after (by componentry of individual grain size classes) decompression-driven fragmentation show not only that crystals influence particular size fractions across the total grain size distribution, but also that free crystals are smaller in the fragmented material than in the original pumice clast. Taken together, our results confirm previous work showing both the control of initial texture on the primary fragmentation process and the contributions of secondary processes to ash formation. Critically, however, our extension of previous analyses to characterization of shape, texture and componentry provides new analytical tools that can be used to assess contributions of secondary processes to ash deposits of uncertain or mixed origin. We illustrate this application with examples from SHV deposits.

Prof Jurgen W Neuberg
Editor: JVGR

June 28, 2016

Re: Revised JVGR Manuscript VOLGEO5083R1

Dear Prof Jurgen Neuberg,

We are pleased that you have elected to accept our manuscript *" Primary and secondary fragmentation of crystal-bearing intermediate magma"*, pending minor revisions, for publication in JVGR. In our attached revision we have addressed all of the suggestions of the referee. All our responses to the particular suggestions can be found in our point-by-point reply.

Thank you for handling this manuscript so efficiently.

Yours truly,

Thomas Jones

Corresponding Author Contact Details:

Thomas Jones
Department of Earth Sciences
Durham University
South Road, Durham, UK, DH1 3LE
t.j.jones@durham.ac.uk

Point-by-point redress of reviewer comments

JVGR submission: Primary and secondary fragmentation of crystal bearing intermediate magma

Manuscript number: VOLGEO5083

Authors: Thomas J. Jones, Keri McNamara, Julia Eychenne, Alison C. Rust, Katharine V. Cashman, Bettina Scheu and Robyn Edwards

Reviewer comments are shown in standard font, responses and respective changes are shown in *red italic font*

Reviewer #1: In this article, the authors used original experimental data to better understand the control of crystals on fragmentation of magma. The paper is very clear and well written and the conclusions are convincing. This field of research is active and many papers have been published in this subject, but the present contribution adds something new to the literature (the detailed analysis of the control of crystals). I thus support its publication in the journal of volcanological and geothermal research. I have only two major points and a couple of minor points the authors may wish to take into account in the final version of the manuscript.

Main points:

(i) In a recent paper, Costa et al. "Assessing tephra total grain-size distribution: Insights from field data analysis", Earth and Planetary Science Letters 443 (2016) 90-107, suggest that the Total Grain Size Distribution of volcanic deposits is better describe by (at least) two subpopulations, a coarse and a fine one, with two different power law exponents. It is my understanding that the present paper deals with the fine population rather than with the coarse one. This may explain the different between the authors' conclusion on the evolution of D (that here remains lower than 3) and the one of Kaminski and Jaupart 1998 (where D becomes larger than 3). It is possible that the effect of crystals is more important on the fine fraction than on the coarse one? Some figures may indicate a larger decrease of the number of the largest fragments in the distribution than predicted by the best fit D exponent. I suggest the authors add a few words on that question in the discussion.

Thank you for highlighting this recent work. In direct response to your question you can see the grain size fractions included in the power-law fit in Figure S1. Where possible we deal with the total grain size distribution collected from the experiments not just a coarse or fine fraction. A maximum of two data points were excluded at either the coarse or fine tail of our experimental data set. We therefore cannot produce multiple fractal dimensions; it would be unreasonable to fit a line between one or two data points. We have added the following sentences to clarify our analysis approach. "In some cases one or two data points are excluded at the coarse or fine tail. The open circles in Figure S1 represent these data points."

Lastly, in response to: "It is my understanding that the present paper deals with the fine population rather than with the coarse one. This may explain the different between the authors' conclusion on the evolution of D (that here remains lower than

3) and the one of Kaminski and Jaupart 1998 (where D becomes larger than 3).” For fractal dimensions (D values) > 3 it is the small grain size fraction that controls the power law. So dealing with the fine fraction cannot be the reason we see a small D value. Only studying the fine grain size fractions should actually act to raise D.

(ii) The application of the model to the SHC deposits is interesting. However it does not allow one to fully entangle the relative contribution of the different parameters that impact the final grain size distribution because the starting material is not exactly the same. I wonder if the analysis can be carried on on samples coming from fall and flow deposits produced by the same eruption, such as MSH 1980. This should help to emphasize the role of secondary fragmentation in the GSD of PDC.
We selected the two SHV events based on their eruption characteristics. The March 1997 event produced a tephra deposit that was entirely formed of co-PDC ash (therefore solely produced by secondary fragmentation). Whereas the September 1997 tephra contains contributions from both vent-derived and co-PDC ash. It should have products from both primary and secondary fragmentation. Using these two events with different eruption characteristics we can investigate the influence of abrasion in PDCs.

These natural data are included as an example of how one could use our analysis on naturally fragmented material. SHV eruptive material was also chosen because we used SHV pumice as the starting material in all our experiments. We have expanded the first paragraph of Section 5.4 to make this rationale clearer. Unfortunately conducting analysis on MSH material would be beyond the scope of this study. Hopefully using the framework which we set out for classifying and identifying primary and secondary fragmentation products future work will investigate tephra deposits like those at MSH.

<u>Minor points:</u>

- The third highlight seems to miss the main verb.

The third highlight is now changed to “We define a milling index (Adherence Factor) that quantifies the degree of abrasion”

- line 61: secondary fragmentation can also occur in the conduit (through collisions)

We have now made this sentence clearer to include subsurface processes. The new sentence reads: “Volcanic ash can form by both primary and secondary processes; the former from volatile driven decompression during magmatic ascent and the latter from processes after the fragmentation front such as pyroclastic density currents (PDCs) and collisions within the conduit.”

- Figure 3: the effect of temperature is the most notable. But I think it is not really discussed in the paper (or I have missed it). Do you have some explanation for the control of temperature on GSD?

We have chosen to simply describe this effect (line 300). We have ideas why temperature induced grain size coarsening occurs, however on a singular pair of results we did not feel there was sufficient evidence to speculate on the cause of this difference.

- line826: ratio rather than ration.

Changed

- figure 10: in this figure pyroclasts all look like crystals (i.e. with no bubbles and with a rectangular shape). This could be misleading.

Shapes have been altered to include more irregular shapes close to the fragmentation front.

Graphical Abstract (for review)

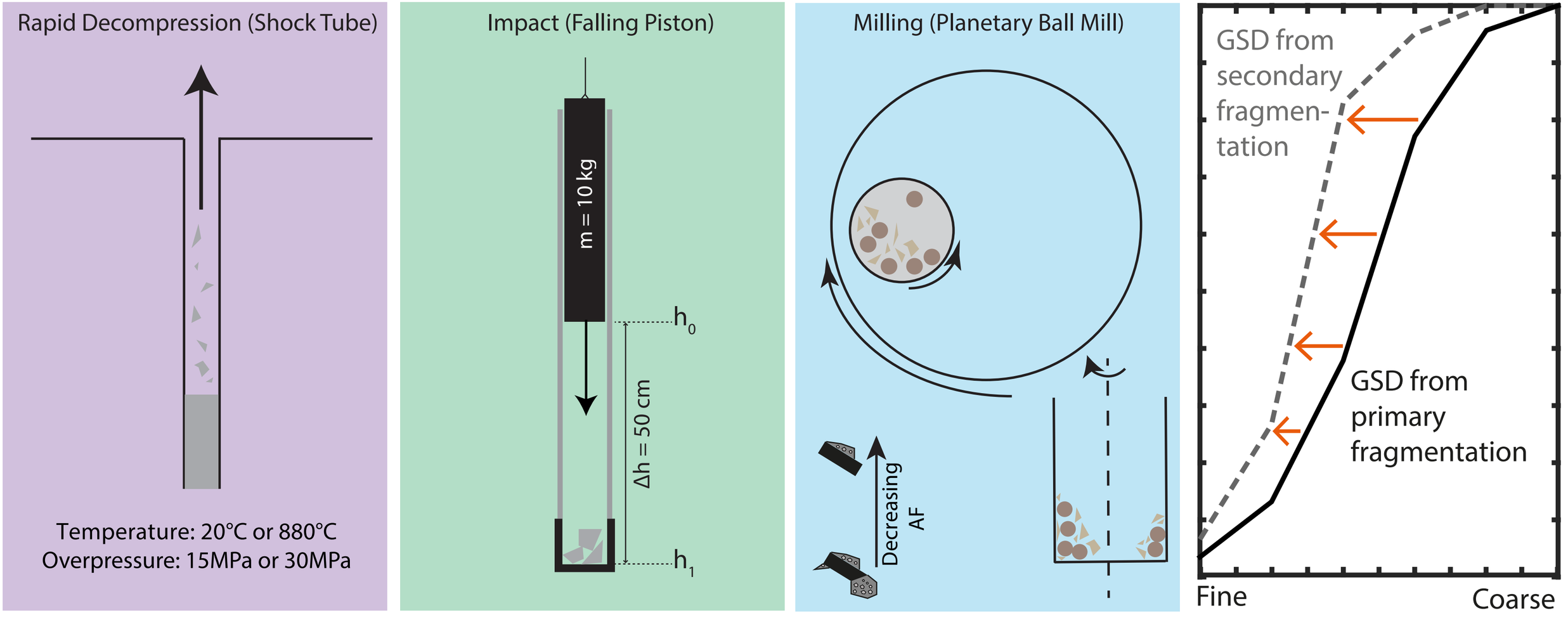

Highlights [each bullet point - maximum 85 characters, including spaces. Max 5 points]

- We investigate ash production with decompression, impact and milling experiments
- Products follow fractal dimensions which are raised by secondary fragmentation
- We define a milling index (Adherence Factor) that quantifies the degree of abrasion
- Crystals provide a control on the GSD at certain size fractions
- Abrasion lowers grain axial ratio and strips adhering matrix from crystals

Primary and secondary fragmentation of crystal bearing intermediate magma

Thomas J. Jones[1,2*], Keri McNamara[2], Julia Eychenne[2], Alison C. Rust[2], Katharine V. Cashman[2], Bettina Scheu[3] and Robyn Edwards[2]

[1] Department of Earth Sciences, Durham University, Durham, DH1 3LE, UK

[2] School of Earth Sciences, University of Bristol, Wills Memorial Building, Bristol, BS8 1RJ, UK

[3] Department of Earth and Environmental Sciences, LMU Munich, Theresienstr. 41, 80333 Munich, Germany

***Corresponding author**: t.j.jones@durham.ac.uk

Abstract

Crystal-rich intermediate magmas are subjected to both primary and secondary fragmentation processes, each of which may produce texturally distinct tephra. Of particular interest for volcanic hazards is the extent to which each process contributes ash to volcanic plumes. One way to address this question is by fragmenting pyroclasts under controlled conditions. We fragmented pumice samples from Soufriere Hills Volcano (SHV), Montserrat, by three methods: rapid decompression in a shock tube-like apparatus, impact by a falling piston, and milling in a ball mill. Grain size distributions of the products reveal that all three mechanisms produce fractal breakage patterns, and that the fractal dimension increases from a minimum of ~2.1 for decompression fragmentation (primary fragmentation) to a maximum of ~ 2.7 by repeated impact (secondary fragmentation). To assess the details of the fragmentation process, we quantified the shape, texture and components of constituent ash particles. Ash shape analysis shows that the axial ratio increases during milling and that particle convexity increases with repeated impacts. We also quantify the extent to which the matrix is separated from the crystals, which shows that secondary processes efficiently remove adhering matrix from crystals, particularly during milling (abrasion). Furthermore, measurements of crystal size distributions before (using x-ray computed tomography) and after (by componentry of individual grain size classes) decompression-driven fragmentation show not only that crystals influence particular size fractions across the total grain size distribution, but also that free crystals are smaller in the fragmented material than in the original pumice clast. Taken together, our results confirm previous work showing both the control of initial texture on the primary fragmentation process and the contributions of secondary processes to ash formation. Critically, however, our extension of previous analyses to characterization of shape, texture and componentry provides new analytical tools that can be used to assess contributions of secondary processes to ash deposits of uncertain or mixed origin. We illustrate this application with examples from SHV deposits.

Keywords: Volcanic ash; Fragmentation; Broken crystals; Milling; Fractals; X-ray computed tomography

1. Introduction

Volcanic ash is an inevitable product of nearly all explosive eruptions. Formed by fragmenting magma and/or rock, it is a particularly important hazard in the modern day, presenting a risk to aviation as well as to human health. Additionally, the associated risk is not confined to areas proximal to the volcano, but, as demonstrated by recent eruptions in Iceland and Chile, can also have far reaching impacts (e.g., Alfano et al., 2011). Understanding the origin of volcanic ash particles is thus critical for predicting the nature and extent of ash hazards. Volcanic ash can form by both primary and secondary processes; the former from volatile-driven decompression during magmatic ascent and the latter from post-fragmentation processes such as collisions within the conduit and transport in pyroclastic density currents (PDCs). Distinguishing between the products of primary and secondary fragmentation is necessary for a comprehensive understanding of volcanic ash deposits.

Primary magmatic fragmentation occurs either through ascent-driven vesiculation and expansion of a volatile phase or by rapid decompression, such as occurs because of edifice collapse. Typical fragmentation studies relate tephra characteristics (e.g., grain size distributions, GSDs) to the energy of the primary fragmentation (e.g. Walker, 1973). Secondary fragmentation further decreases the average grain size of a pyroclastic deposit. In PDCs, secondary ash-forming processes include both impact and abrasion (e.g. Freundt and Schmincke, 1992), which cause fining of vent-derived particles with increased transport distance (Dufek and Manga, 2008; Kueppers et al., 2012). The total grain size distribution (TGSD) produced by primary and secondary fragmentation processes, in turn, affects the efficiency of heat transfer (e.g., Zimanowski et al., 2003), PDC mobility (Félix and Thomas, 2004) and formation of co-PDC plumes (Eychenne et al., 2012). For this reason, identifying the contributions of co-PDC ash to the total deposit is particularly important for modelling ash plumes, especially in large eruptions where such deposits may make up a large proportion of distal ash (e.g. Dartevelle et al., 2002; Cashman and Rust, 2016; Engwell and Eychenne, 2016; Engwell et al., 2014; Eychenne et al., 2015; Eychenne et al., 2012; Rose and Durant, 2009). The goal of our work is to develop analytical tools to distinguish primary from secondary ash deposits.

Controlled laboratory experiments have provided some links between natural variables (e.g. degree of overpressure, transport distance) and the characteristics of the associated tephra deposit. Laboratory study of primary fragmentation is typically performed by shock-tube experimentation at magmatic temperatures. Results show that for a given sample porosity, greater degrees of overpressure increase the fragmentation efficiency and thus decrease the overall grain size (Kueppers et al., 2006b). Experimental GSDs typically follow power-law distributions with fractal dimensions (D) of ~2.5 (Kueppers et al., 2006a). Variations about this value are thought to reflect the energy of fragmentation, with higher fragmentation energies producing deposits with higher D values (Perugini and Kueppers, 2012). The fractal dimension increases by secondary fragmentation (Kaminski and Jaupart, 1998). The effects of secondary fragmentation have been quantified using experiments involving both collision and abrasion (Cagnoli and Manga, 2004; Mueller et al., 2015). Results confirm that the fine ash content increases with time, and that experiments involving abrasion produce finer ash than experiments involving impact (Mueller et al., 2015). Also important is the original clast density, with grain size reduction dominated by breakage of the more vesicular fragments (Kueppers et al., 2012). This observation has particular relevance to explosively generated ash, which often has TGSDs dictated by the vesicle size distribution (Genareau et al., 2012; Liu et al., 2015a; Rust and Cashman, 2011).

Less well studied is the role of crystals in fragmentation and ash formation. Crystals commonly form a major constituent of intermediate magmas; thus it seems likely that the abundance and size distributions of crystals would affect the size, density and shape of explosively generated fragments. In fact, crystal concentrations in ash deposits show that individual crystals typically have a limited size and density range (e.g., Martel et al., 2001; Cashman and Rust, 2016; Sparks and Walker, 1977). Crystals in ash fractions are often broken or rounded, possibly due to the fragmentation and/or ash generation mechanism (e.g. Bachmann et al., 2002; Best and Christiansen, 1997; Carter et al., 1986). The presence of broken crystals in explosive eruption deposits has previously been attributed to two main processes: melt inclusion (MI) decrepitation and shock fragmentation. Fragmentation by MI decrepitation occurs when overpressure in the MI exceeds the tensile strength of the crystal. This may

be achieved by cyclic periods of overheating linked to the latent heat of crystallisation (Bindeman, 2005; Zhang, 1998) or rapid decompression of crystal-bearing magma during ascent (Best and Christiansen, 1997; Bindeman, 2005; Miwa and Geshi, 2012; Tait, 1992; Williamson et al., 2010). Crystal fragmentation by shock fragmentation can occur by extensional fracture during decompression and subsequent melt vesiculation (Chouet et al., 1994; Kennedy et al., 2005; Miwa and Geshi, 2012; Pallister et al., 1996).

Here we present a multi-component analysis of experimentally fragmented pumice samples. Although the effects of both rapid decompression and abrasion have been previously investigated, we extend these experiments in several important ways. First, we focus on fragmentation of a vesicle- and crystal-rich intermediate magma by a range of methods. Second, we explore the effects of both primary and secondary fragmentation on the resulting shape, size and componentry of the particle population. Primary fragmentation is simulated by rapid decompression experiments in a shock tube while secondary processes (such as abrasion and impact in PDCs) are simulated in the laboratory by ball mill and falling piston experiments, respectively. Controlled experiments with the same starting material – pumice from recent eruptions of the Soufriere Hills Volcano (SHV) – allow us to compare the ash-generating efficiency of the different processes. Additionally, adding componentry analysis allows us to evaluate the extent to which (broken) crystals affect the grain size, shape and fractal dimension of the tephra deposit. Finally, we compare our experimental results with natural SHV ash samples from fallout deposits produced by a dome collapse and a Vulcanian eruption.

2. Methods

All experiments were conducted using a single crystalline andesite pumice block that survived decompression during an explosive (Vulcanian) eruption of SHV in February 2010. We fragmented the pumice sub-samples in three different ways: rapid decompression at both room temperature and 880˚C, impact and milling at room temperature - all within the brittle deformation field; (Alidibirov and Dingwell, 2000). To characterize the resulting material, we determined the total grain size distributions produced by each fragmentation method, as well as ash components, shapes and textures.

For the decompression experiments, we also compare crystal sizes and shapes before and after fragmentation.

2.1 Pre-fragmentation characterisation

The original sample had a dense-rock equivalent density of 2.69×10^3 kg m^{-3} and an estimated glass transition temperature (T_g) of ~790°C (Jones et al., 2013). For the decompression experiments we drilled four pumice cylinders, each measuring 60 mm long and ~25 mm in diameter. Prior to fragmentation the physical and textural properties were characterised. Crystal populations and pre-existing crystal fractures were quantified with X-Ray computed tomography (XRCT) and optical microscopy of thin sections; helium pycnometry was used to calculate connected and total porosities for the four samples (see Table 1).

2.1.1 X-Ray computed Tomography

Radiographs for XRCT were collected with a Nikon Meterology 225/320kV Custom Bay scanner located at the Henry Mosely X-Ray Imaging Facility, University of Manchester. Acquisition conditions were 41 kV accelerating voltage, 239 μA current and a 0.5 mm Al filter. An exposure time of 1000 ms was used for all scans. To reconstruct the scans, we first calculated the centre of rotation of all the radiographs and then applied a beam hardening correction using the Xtek CT Pro software.

All processing was conducted using the 3D visualization and segmentation software Avizo 8.0 Standard. Crystal volumes were determined from a sub-volume of ~ 2.5×10^8 voxels extracted from the raw image stack, where 1 voxel measures 0.02257 mm^3. A 3x3x3 voxel 3D median filter was applied to this sub-volume with three iterations. Each image in the stack was segmented and thresholded to identify phases based on their characteristic grey scale values. A binary data set was then created to generate either the surface or volume of the segmented crystals. Only objects of 5 voxels or larger were included in calculations of crystal volumes. The separation of pre-broken crystal fragments can be achieved when distances are > ~ 0.09 mm.

Mineral modes, porosity and bulk sample crystallinity were determined with a larger sub-volume of $6x10^8$ voxels, which required significantly more computational capacity than the crystal volume measurements, and therefore a different approach. Firstly a median filter was applied to the entire image stack with ImageJ software (http://rsbweb.nih.gov/ij/). Next pores and mafic and felsic mineral phases in each image were separated based on grey scale values with an ImageJ plugin, PhaseQuant (Elangovan et al., 2012). The small density variation between different mineral phases, and the corresponding similarity of grey scales, made segmentation of specific minerals difficult so crystals are classified as either mafic or felsic phases (e.g. Cnudde et al., 2006). Each segmented volume (felsic, mafic and pores) was then converted into a binary image stack and imported into Avizo. The felsic crystal data required a 3D erosion and subsequent dilation by two voxels to remove background noise. Finally, surface generation and volume analysis was performed.

2.1.2 Textural characterisation

A 3D rendered volume of an example sub-sampled volume (Figure 1a) shows the distribution of crystals prior to experimental fragmentation. Broken crystals are common, and often have a jigsaw-like fit. Where the separation between these crystal fragments was sufficient to resolve in the tomographic analysis, each crystal fragment was counted as a separate crystal. The average DRE crystallinity for crystals >32µm in diameter (5 φ) is 27 vol. % with ~21% felsic and ~6% mafic crystals and oxides. Point counts of petrographic thin sections of the same samples included smaller microlites, and thus yield a higher crystallinity (38%); this shows that about 11% of the total crystal volume is < 32 µm.

A crystal volume distribution (CVD) extracted from the rendered tomographic volumes is shown in Figure 1b. The crystals range in size from 10^{-5} to 10^{1} mm^3, with a mode of 10^{-3} mm^3. Measurement of broken crystals as individual fragments means that the rendered volume distribution accounts for pre-existing crystal breakage prior to experimental fragmentation, within the resolution of the imaging technique.

193

194 *2.3 Porosities and fragmentation threshold*

195 Porosity provides information about the potential energy available for fragmentation during
196 decompression (Kueppers et al., 2006b) and is used to calculate the minimum initial overpressure
197 required for complete fragmentation in the decompression experiments (Spieler et al., 2004). To
198 measure porosity, we cleaned the sample cores and measured their porosity by helium pycnometry,
199 using a Quantachrome Instruments Ultrapync 1200e pycnometer housed at LMU Munich, Germany.
200 Total porosity ϕ_t was calculated from the solid density ρ_s and the bulk sample density ρ as:

201 $$\phi_t = 1 - \frac{\rho}{\rho_s}, \qquad [1]$$

202 where ρ_s is the measured density of powdered sample milled to a grain size less than the minimum
203 pore size. The connected or open porosity ϕ_c is calculated as:

204 $$\phi_c = \left(\frac{V_C - V_M}{V_C}\right) \times 100 \text{ , } [2]$$

205 where V_C is the geometrical volume of the cylindrical samples and V_M is the volume measured by He
206 pycnometry. The isolated (closed) porosity, ϕ_i can then be defined as:

207 $$\phi_i = \phi_t - \phi_c. \qquad [3]$$

208

209 The average total porosity is 66%, with a range of 1.25% between all sample cores. Individual
210 porosity values for the cores used in the four rapid decompression experiments are reported in Table
211 1.

212

213 *2.2 Experimental fragmentation*

214 Samples from the Soufriere Hills Volcano (SHV) were fragmented experimentally by three methods:
215 rapid decompression, hammer impacts and ball milling (Figure 2). Broadly, these aimed to replicate
216 three natural volcanic processes: magmatic overpressure and decompression, impact and abrasion/
217 milling in turbulent flow.

218 Rapid decompression-driven fragmentation was performed using a shock tube-like apparatus
219 (Figure 2a) at the LMU Munich, Germany (e.g. Scheu et al., 2008; Spieler et al., 2004). By using two

220 experimentally calibrated diaphragms we achieved a pressure differential of either 15 or 30 MPa; this
221 exceeds the fragmentation threshold by 12 and 27 MPa (Spieler et al., 2004). At each differential
222 pressure, experimental fragmentation was conducted at both 20˚C and 880ºC. The experimentally
223 generated pyroclasts were left to settle in the low pressure tank for 1-2 hours and then sieved to 125
224 µm using a pressure washer filled with distilled water. All material that passed through the 125 µm
225 sieve was left to settle for 2 days in a sediment collection tank.
226 Impact experiments were performed by placing a single rectangular block (~ 4 x 5 x 2cm) of
227 SHV pumice into a detachable steel cup, as illustrated in Figure 2b. A 10 kg steel piston was then
228 repeatedly dropped from a height of 50 cm. The fives experimental runs, each run with a different
229 block, comprised 5, 10, 15, 20 and 25 piston drops; at the end of each run the entire sample was
230 recovered from the basal cup by flushing with distilled water.
231 Ball mill grinding was performed using a Planetary Ball Mill PM 100 manufactured by
232 RETSCH Ltd. The initial GSD for the ball mill experiments, represented by "0 min" in Figure 3c, was
233 created by crushing ~ 10cm square blocks of SHV pumice. For each experiment an aliquot of this
234 input sample was weighed and placed into the agate jar of the ball mill (Figure 2c) along with six 1.6
235 cm diameter agate balls. The container was sealed and rotated at 450 rpm for 0.5, 1, 2.5 or 5 minutes,
236 and the sample removed for subsequent analysis.
237
238 *2.3 Post-fragmentation characterisation*
239 After fragmentation by the three methods (Figure 2) the experimental pyroclasts were
240 characterised by grain size, componentry, shape and fracture surface morphology.
241
242 *2.3.1 GSD measurements*
243 All particles coarser than 125 µm were separated into grain size fractions by manual sieving
244 into size bins of -3, -2, -1, 0, 1, 2, 3 phi (φ). Particle size analysis for material ≤ 250 µm was
245 performed at the Environmental Change Laboratory, University of Western England, Bristol, UK
246 using a Mastersizer 2000 laser diffraction particle size analyser, manufactured by Malvern

247 Instruments Ltd. Sieve and Mastersizer data were combined using the overlapping 3 φ size fraction to
248 produce a total grain size distribution for each fragmentation experiment.
249
250 *2.3.2 Componentry*
251 Componentry analysis was conducted under a binocular microscope for grain sizes -3 to 3 ϕ.
252 Grains ≥ 500 μm were picked manually; smaller grains were classified from analysis of digital
253 microscope images. Where possible, at least 300 grains were analysed for each grain size fraction.
254 Grains were separated into three component categories: (1) free mafic crystals, (2) free felsic crystals,
255 and (3) clasts (i.e. anything that is not a free crystal), where a free crystal is defined as having matrix
256 adhered to less than 20% of the surface of the crystal. Additional 2D componentry of the 2 φ ash
257 fraction was performed using backscattered electron (BSE) mode of Scanning Electron Microscopy
258 (SEM) on a Hitachi S-3500N SEM at the School of Earth Sciences, University of Bristol. This grain
259 size fraction was chosen for detailed analysis because all experiments produce sufficient samples of
260 this size fraction. Ash grains were set in resin and polished to expose grain interiors before being
261 carbon coated. A mosaic of 25 images was taken of each sample using BSE mode from a working
262 distance of 18 mm, a 15Kv accelerated voltage and a magnification of 60x. Each image had a 1024 x
263 768 pixel resolution. Componentry was performed manually by placing a grid on the image and
264 counting grains. Grains were subdivided into three components: (1) crystals with no attached matrix,
265 (2) crystals with matrix attached, and (3) vesicular matrix clasts (all matrix grains were vesicular).
266 The 3D morphology of fine ash samples was examined using secondary electron mode on the
267 SEM. Ash grains within the 2 φ sieve fraction were mounted on carbon-based stubs and Au coated to
268 a thickness of approximately 5 nm. For grains measuring 125-250 μm or 3 φ (the finest fraction
269 studied), silver paint was applied to the SEM stub prior to Au coating, to reduce the effects of
270 charging.
271
272 *3.2.3 Shape analysis*
273 The 2D SEM image mosaics of the 2 φ grain size fraction were analysed with ImageJ
274 software. Images of individual grains were thresholded and converted to binary format before

quantifying grain shapes using axial ratio and convexity. Only grains from the 'vesicular matrix' componentry category were analysed for shape as they displayed the most variation between sample runs. This component comprised between 10 and 60 % of the total depending on the fragmentation mechanism.

Axial ratio is the ratio of the axes of the particle's best-fit ellipse:

$$\text{Axial ratio} = \frac{\text{Major axis}}{\text{Minor axis}}. \quad [4]$$

Convexity is defined as the ratio of the perimeter of the grain and its convex hull (the smallest convex polygon that contains the 2D shape):

$$\text{Convexity} = \frac{\text{Perimeter of convex hull}}{\text{Perimeter}}. \quad [5]$$

It is a measure of the surface roughness of the external shape boundary (Liu et al., 2015b), such that a high value of convexity indicates a smooth external surface.

Where a crystal comprised at least 10% of the entire grain, areas of crystals and matrix were also calculated separately by manually varying the greyscale threshold to generate separate binary images, then calculating the pixel area of each. Abrasion is expected to decrease the relative proportion of glassy matrix adhering to crystals. For this reason, Meyer (1971) define the "abrasion index", which is the ratio of the area of a crystal to the area of attached matrix. However, abrasion may not be the only process to affect the crystal-matrix ratio. Furthermore, Meyer's "abrasion index" is unbounded (i.e. becomes infinite if there is no matrix). For these reasons, we introduce a related parameter we call the Adherence Factor:

$$\text{Adherence factor (AF)} = \frac{\text{Area of crystal}}{\text{Area of crystal} + \text{Area of matrix}} \quad [6]$$

The adherence factor is bounded between one (matrix only with no dominant crystal) and zero (for a crystal with no adhered matrix) and therefore we expect AF to decrease with increasing abrasion.

4. Results

298 *4.1 Grain size distributions*

299 The grain size distributions (GSD) of all sample sets are limited to a maximum of -3φ because
300 of initial sample size. Rapid decompression (Figure 3a) creates a sample suite with a median size of -
301 2.30φ to 0.23φ. Most striking is the effect of changing fragmentation temperature, where elevated
302 temperatures yield coarser GSDs. The grain size distributions produced from the falling piston
303 experiments are notably more fine-grained than pyroclasts produced by rapid decompression. Median
304 sizes range from 1.70φ to 5.03φ and generally decrease with increased number of hits (Figure 3b).
305 The grain size resulting from 10 hits, however, is abnormally small relative to the other data sets; we
306 attribute this to natural heterogeneity within the pumice block that was the source of the starting
307 material of each experiment. Experimentally generated pyroclasts from ball milling show a systematic
308 increase in fine particles with increased milling duration. All GSDs produced by milling show a
309 pronounced fine tail and are skewed to smaller sizes than GSDs from the rapid decompression and
310 falling piston experiments.

311

312 *4.2 Ash shape*

313 Vesicular grains (i.e. all those that were not dominated by a single large crystal of over 10%
314 of the total grain) were analysed for two shape parameters: axial ratio and convexity. Axial ratio is a
315 representation of particle elongation, while convexity quantifies the smoothness of the grain exterior
316 (Liu et al., 2015b). Axial ratio values vary considerably depending on the experimental fragmentation
317 method (Figure 4a-c). Ash produced by rapid decompression has a greater range of axial ratio values
318 than those produced by milling or impact. Ash grains from the milling experiments showed the
319 smallest range of axial ratios although the range increased with milling time: axial ratios of grains
320 milled for 1 minute have a lower mode and extend to larger values than axial ratios of grains milled
321 for 0.5 minutes (Figure 4c). In contrast, axial ratio values changed little with number of impacts
322 (Figure 4b). However, convexity data show that increased impacts smoothed out the irregular grain
323 surfaces in the comparative grain size fraction: the ash grains produced by 10 piston impacts have
324 greater average convexity values, and thus less irregular exteriors, than grains produced by 5 impacts
325 (Figure 4e).

326

327 *4.3 Experimentally generated pyroclast componentry*

328 Componentry analysis of the pyroclasts generated by rapid-decompression required the proportions of
329 free mafic and felsic crystals (those with < 20% adhered matrix) to be discriminated from other matrix
330 dominated clasts (Figure 5a). No free crystals were observed at grain sizes greater than -1 φ. At finer
331 grain sizes the proportion of crystals varies considerably for different grain size fractions. Within
332 these coarse-grained rapid decompression products, free crystals (mainly felsic) are most abundant in
333 the 1φ size fraction, contributing ~40 weight % to this grain size bin. The maximum abundance of
334 mafic crystals varies between 1 and 2 φ for different experimental runs. We observed no systematic
335 componentry changes in the decompression experiments (Fig. 5a) as a function of either ΔP or
336 fragmentation temperature; the small variations between experimental runs likely relate to slight
337 sample heterogeneities prior to experimental fragmentation.

338

339 Within the 2φ fraction (Fig. 5b), there are only small differences in SEM componentry between the
340 hot and cold rapid decompression products. Both have similar proportion of free crystals (with no
341 attached matrix) although there is a higher proportion of crystals with attached matrix in the products
342 of hot decompression (Figure 5b). More dramatic is the comparison with data from other
343 fragmentation mechanisms, where products of the milling and impact experiments show a higher
344 proportion of free crystals than the decompression products. Additionally, the sample milled for
345 longer (1 min) has a higher proportion of free crystals than its counterpart that was milled for 30
346 seconds. A similar trend is observed in the impact products: the sample that underwent 10 hits has a
347 greater proportion of free crystals than the sample that was hit five times. These observations show
348 that repeated fragmentation removes crystal coatings and frees individual crystals from the matrix.

349

350 *4.4 Crystal volume distributions*

351 The crystal populations within the original SHV pumice cores and the pyroclasts produced by rapid
352 decompression were quantified by analysis of X-Ray CT (Figure 1) and SEM analysis (Figure 5a),
353 respectively. To effectively compare these pre-experiment and post-experiment crystal populations,

354 the crystal volume distributions generated by X-Ray-CT were converted to a length scale. We assume
355 that all crystals within the volcanic rock samples form euhedral cuboid volumes,

356 $$\square_{\square\square\square} = h \times \square \times \square \quad [7]$$

357 where *h* and *w* represent the height and width of the smallest crystal face and *l* is length. Assuming
358 that crystals have aspect ratios of 2:1 and that the minor and intermediate axes are the restrictive
359 dimensions of the sieve size (*d*), an effective particle diameter is calculated as:

360 $$\square = \left(\frac{\square_{\square\square\square}}{2}\right)^{1/3} \quad [8]$$

361 Effective diameters are converted to the φ scale, the volumes falling in each φ bin summed and
362 converted to weight % to form the "Rock" data set in Figure 6.
363
364 The crystal population generated by decompression is determined by averaging the mass of
365 mafic/felsic crystals within each size fraction of all decompression experiments. We average because
366 no significant difference in componentry was observed when changing fragmentation overpressure or
367 temperature. These data are then converted to weight % of total crystals and form the "Ash" data set
368 in Figure 6.
369
370 The size distribution of crystals within the ash relative to those in the SHV pumice (Figure 6) shows
371 that rapid decompression caused the crystal size to decrease. Grain size reduction is concentrated
372 over the central portion of the size range investigated. In coarser grain size fractions (2 - 0 φ) the
373 crystal abundance in the pumice is greater than the abundance in the ash and is dominated by felsic
374 crystals. Conversely, in the finer fractions (1 - 3 φ) crystals are more abundant in the ash than in the
375 original pumice. Moreover, there are no crystals within the -2φ ash fraction, although they were
376 present in the pumice prior to decompression and fragmentation. This suggests that crystals were not
377 simply freed from the matrix during fragmentation but were also reduced in size by crystal breakage.
378
379 *4.5 SEM imagery of fracture surfaces*

Photomicrographs of the 2φ ash fraction produced by rapid decompression reveal characteristics of broken crystal surfaces (Figure 7) that can be classified as: (1) smooth, clean surfaces with negligible topographic relief (Figure 7a) and (2) rougher, often highly irregular surfaces displaying intense river-line fracturing and hackles (Figures 7c and 7d). On some crystals, a vesicular glass coating is observed (Figure 7b); it is slightly more common in the hot fragmentation experiments relative to the room temperature runs. No other differences were observed in the fracture surfaces or styles between the products of hot and cold experiments. About 90% of broken crystals have clean broken surfaces with negligible topographic relief. We interpret these as breakage along a cleavage plane or a pre-existing internal fracture (Figure 7a). Where river-line fractures are observed on these surfaces they are widely spaced and have low relief. Only about 10% of broken crystal surfaces are much rougher and complex due to fractures cross-cutting cleavage planes (e.g. Figure 7d).

Finally, sub-circular cavities, including some with protruding glass strands, are a rare but ubiquitous feature of crystal surfaces in the experimental products. Similar features were observed by Williamson et al. (2010) in natural SHV pumice and interpreted as melt inclusions that burst within a plastic groundmass due to a major decompression event (e.g. dome collapse). Melt extension is a non-brittle process that could not have been generated through experimental fragmentation at room temperature. The fact that we observe these features in the experiment products indicates that they must already have existed in the dome/pumice samples prior to decompression in the laboratory.

5. Discussion

We have explored several techniques to characterise both experimentally generated ash and its parent material (Table 1). We now use these results - from grain size measurements, fractal analysis, componentry and shape descriptors - to examine the effects of different fragmentation mechanisms on pyroclast characteristics. For samples that were rapidly decompressed, we couple this analysis with XRCT and SE SEM imagery to examine how rapid decompression-driven fragmentation alters the crystal population. Lastly, to illustrate our techniques we compare experimentally generated SHV ash to two natural SHV ash examples.

408

409 *5.1 Fractal behaviour of products*

410 Since the idea of fractal behaviour was introduced to Earth Sciences (e.g., Korvin, 1992; Turcotte,
411 1986), power law exponents (fractal dimension D values) have been used to quantify the size
412 distributions of volcanic pyroclastic products (e.g., Kaminski and Jaupart, 1998; Perugini et al., 2011;
413 Taddeucci et al., 2004). Higher power law exponents represent tephra deposits that are dominated by
414 finer ash fractions. Therefore fractal dimensions are commonly used to infer the fragmentation
415 efficiency and have been linked to the energy available for fragmentation (e.g., Kueppers et al.,
416 2006a).

417

418 It has long been noted that tephra produced from volcanic eruptions commonly has a much higher
419 fractal dimension (larger fine ash component) than expected from simple crushing or rock
420 disaggregation (Hartmann, 1969). The source of this fine ash is an open question, but is clearly
421 dictated ultimately by the vesicle size distribution (Rust and Cashman, 2011). Kaminski and Jaupart
422 (1998) proposed a model of secondary fragmentation based on experimental fragmentation, where
423 they assumed that piston impact causes primary fragmentation while grinding in a ball-mill caused
424 secondary fragmentation. In this scenario, primary fragmentation initially creates $D=2.5\pm0.1$, then
425 ongoing selective re-fragmentation through particle-particle collisions increases the values of $D \geq 3$
426 preserved in fall deposits. However, many experimental fragmentation experiments fail to replicate
427 the high power law exponents observed in natural pyroclastic deposits (Table 2). This leads to a
428 question about the mechanism(s) capable of producing the finer ash, particularly the role of the
429 original bubble population in controlling the final grain size distribution (Rust and Cashman, 2011).

430

431 We analysed the fractal dimension of the total GSD for all experimental fragmentation methods by
432 converting raw data (mass proportion of particles in different size bins; Figure 3) to number-based
433 data to aid comparison to other published data sets (e.g. Kueppers et al., 2006a). Over the size range
434 analysed here, all experimentally produced ash samples follow a power law distribution, that is, they
435 plot on a straight line in log(N)–log(L) space (Figure 8), where N represents the number of grains

436 larger than corresponding fragment size (L) and the slope defines the fractal dimension (D). The
437 power-law distributions were fitted to the total GSD recovered from the experiments. In some cases
438 one or two data points are excluded at the coarse or fine tail (open circles in Figure S1).
439
440 The log(N) vs. log(L) data for the rapid decompression experiments (Figure 8a) form linear trends
441 with fractal dimensions between 2.03 and 2.24, in good agreement with other studies that have used
442 the same fragmentation method (Kueppers et al., 2006a; Kueppers et al., 2006b; Perugini and
443 Kueppers, 2012). Pyroclasts from the impact (falling piston) experiments also show a fractal
444 distribution (Figure 8b) with a mean D = 2.60. This value is comparable to values from simple
445 crushing and disaggregation of rocks (Table 2; Hartman, 1969). The falling piston sample set shows
446 the most variation. Here D values do not vary systematically with number of impacts, although the
447 power law exponents do broadly increase with increased number of impacts. In these analyses, we
448 excluded the tails of the fragment size distribution when calculating D (represented as open circles in
449 Figure S1), which may account for minor disparities. The milling experiments follow a power law
450 distribution, which shows a systematic increase in D from 2.33 at 0.5 min to 2.45 at 5 mins (Figure
451 8c). This progressive rise in D suggests that milling not only creates fine ash but also causes the fine
452 ash component to become increasingly dominant in the TGSD.
453
454 Our experimental data show that secondary fragmentation can progressively increase D from an initial
455 value resembling rapid decompression-driven fragmentation to higher values. Yet, even after
456 considerable milling durations (5mins) or a large number (25) of successive impacts, the experimental
457 products do not exceed D values of 3. Furthermore, analysis of the 2φ fraction shows that the crystals
458 were not being broken through milling, rather they were being stripped of adhering groundmass. This
459 suggests that during secondary fragmentation of crystal rich tephra, the crystal population may help to
460 sustain a relatively coarse control on the GSD. This interpretation is supported by data from eruptions
461 of Heimaey, Fuego and Oshima, where the basaltic pyroclasts are rich in microphenocrysts and the
462 TGSDs have fractal dimensions D~1.9-2.3. Silicic deposits (Mount St. Helens, El Chichon and
463 Quizapu), in contrast, have both low (or no) groundmass crystallinity and D values >3 (Table 2).

464 Assuming all of the eruptions listed in Table 2 involved secondary, as well as primary, fragmentation
465 (through both milling and impacts, either with the conduit wall or within the particle-rich plume at
466 depth), the differences in observed D seem most easily explained by variations in groundmass
467 crystallinity. Where large proportions of crystals are present in the starting magma they provide a
468 coarse control on the grain size distribution and prevent production of high proportions of fine ash;
469 this keeps D values low (< 3). The 'final' D value is therefore a function of both magma and
470 fragmentation characteristics, including magma porosity and permeability, magma crystallinity,
471 fragmentation overpressure and the degree of mechanical processing.
472

473 *5.2 Fragmentation control on pyroclast characteristics*

474 Our analysis confirms results from previous experimental studies, including the effect of mechanical
475 fragmentation in shifting the GSD to smaller sizes (Cagnoli and Manga, 2004; Kueppers et al., 2012;
476 Mueller et al., 2015) and the high efficiency of abrasion relative to impact experiments in producing
477 fine ash (Mueller et al., 2015; Figure 3). We also found that the proportion of vesicular fragments
478 decreased with increased milling time and number of impacts (Figure 5b), consistent with Kueppers et
479 al. (2012).

480 Our experiments also show that the mechanism of fragmentation has a significant effect on the
481 characteristics of individual pyroclasts. Of particular note is the variation in the axial ratios of matrix
482 fragments between the three fragmentation mechanisms studied (Figure 4). The axial ratios of impact
483 and milling products are large compared to the decompression products, which suggests that increased
484 mechanical abrasion prevents, or rapidly reduces, the likelihood of producing elongated fragments.
485 Additional milling further increases the mean and range of axial ratio values of ash particles. This is
486 interesting because the small ash particles mimic shape variations previously observed in larger
487 pumice clasts, both in rock tumbling experiments and natural PDC deposits (e.g., Manga et al., 2011).
488 Studies of pumice clast rounding further suggest that both rounding and ash production via
489 comminution are most efficient proximal to volcanic vents, where PDCs are most energetic.

A sizeable portion of the experimental products includes crystals with adhered matrix (Fig. 5b). Past studies have used these fragments as a marker for the amount of abrasion (Freundt and Schmincke, 1992; Meyer, 1971). We quantified this effect using an 'Adherence Factor' (AF: Equation 6; Figure 9). Our data show that the decompression experiments have a substantially higher AF (more adhered matrix) than the products of impact and milling. Hot decompression causes particles to retain slightly more matrix material than cold decompression. Interestingly, increasing the number of impacts or time of milling does not appear to dramatically alter the AF, but the products of milling have a lower AF, overall, than the products of impact.

To interpret the mechanisms responsible for adhered matrix produced by different fragmentation methods, it is also important to consider the effect of crystal breakage on AF. We identified broken crystals by recording whether the crystal displayed at least one intact ring of zoning or whether the zoning was interrupted. In the products of rapid decompression, the crystals with a lower AF value were typically broken. However, there is no obvious correlation between crystal breakage and AF in the products of milling and impacts (Figure S2); this lack of correlation may be due to these two mechanisms not dramatically increasing the number of broken crystals. As a consequence, the matrix is stripped from the outside without breaking the crystal, resulting in many whole crystals with a low AF value. In contrast, the low AF of broken crystals within products of rapid decompression suggests that, as crystals break, internal crystal surfaces are exposed and the area of adhered matrix decreases. Therefore we suggest crystal breakage is the main mechanism for reducing AF during rapid decompression.

5.3 The influence of crystals on fragmentation during rapid decompression

Crystals commonly form a major constituent of erupting magmas and there is the potential for the abundance and size distributions of crystals to affect the size, density and shape of fragments generated in explosive eruptions. The componentry analysis presented here demonstrates that free crystals contribute a significant mass (up to 40%) to specific grain size fractions produced by rapid decompression (Figure 5a). The size range in which crystals dominate appears independent of

517 fragmentation pressure and temperature and is directly related to the crystal size distribution in the
518 starting material. Over the grain size range studied (-3 to 3 φ), plagioclase dominates the total crystal
519 population within each size fraction of the experimentally generated fragments. This agrees with
520 modal analysis of the starting material that showed it to be the most abundant mineral. As illustrated
521 in Figure 5a, free crystals are non-existent or of trivial abundance in the grain size fractions coarser
522 than 0 φ, consistent with the initial crystal size population in the starting material (Rock curve in
523 Fig.6). The mafic crystals show a broader peak at smaller grain sizes, which is likely related to the
524 initial size populations. Therefore the textural characteristics of the starting volcanic material (magma
525 analogue) directly control the experimentally produced tephra (PDC analogue).
526
527 High proportions of crystals within a grain size fraction have the potential to alter the bulk ash
528 density, especially at coarser grain sizes. This, in turn, will cause differential settling of crystals
529 relative to glass fragments of similar size, particularly if the glass is vesicular (e.g., Sparks and
530 Walker, 1977). This effect has been documented in natural eruptive products of Mount St Helens and
531 Quizapu (Cashman and Rust, 2016), where the proportion of free crystals decreases faster with
532 distance from the vent than pumice or glass shards from the same eruption. Currently, ash dispersion
533 models (e.g. Tephra 2; Bonadonna et al., 2010) commonly use a single vesicular glass ash density to
534 represent all grain size fractions from a volcanic eruption. Improvements could therefore be made to
535 more accurately represent crystal-rich pyroclasts, particularly in eruptions characterised by PDCs.
536
537 Crystal size distributions may also help to explain the production of crystal pyroclasts devoid of glass
538 coatings. If a whole (micro)phenocryst were to be extracted from the fragmenting magma, the surface
539 would likely be at least partially coated in a glass. However, if internal broken fragments of a once
540 larger phenocryst are extracted, then the relative chance of a glass-coated surface is low. Knowing the
541 surface properties of ash has implications for remote sensing applications and surface leachate studies.
542 Our componentry study suggests that free crystals in the ash generated by rapid decompression
543 represent broken fragments from once larger whole crystals; this is likely because during rapid

544 decompression fragmentation, the crystals cannot accommodate deformation and hence fracture
545 (Cordonnier et al., 2009).
546
547 Crystal fracture topographies indicate that breaking of crystals in our decompression experiments was
548 dominantly along cleavage surfaces (type 1 fractures) with only about 10% of fractures cross-cutting
549 cleavage planes (Figure 7). Crystals tend to break or 'cleave' along a particular crystallographic
550 orientation because cleavage planes have a relatively low surface energy (Hull, 1999; Kelly and
551 Macmillan, 1986). Experimental studies and natural observations of plagioclase identify intra-
552 crystalline fractures controlled by crystallography and preferential fracture along cleavage planes (e.g.
553 Borg and Heard, 1970; Brown and Macaudiére, 1984). Further, Kennedy et al. (2005) use fractures in
554 SHV hornblende crystals to infer the orientation of tensile unloading and therefore the shape of the
555 fragmentation front. Under mode I tensile failure, cleavage surfaces have a direct and primary effect
556 on fragmentation behaviour. When cleavage planes are orientated perpendicular to the tensile force
557 (parallel to the unloading wave) then simple cleavage fracture is expected to occur (e.g., Figure 7a).
558 However, when cleavage planes are orientated obliquely to tensile forces, then mode II failure can aid
559 fracture by the formation of shear couples (Figure 7c). Therefore, the orientation angle, defined as the
560 angle between the cleavage plane and the tensile force vector, will influence the relative proportions
561 of mode I and II failure.
562
563 *5.4 Comparison with natural samples*
564 To compare with our experimental results, we also studied two ash samples from fallout deposits
565 produced by a dome collapse event (on 31 March 1997) and a Vulcanian eruption (on 26 September
566 1997) of Soufriere Hills Volcano. The dome collapse event generated PDCs but no plume at the vent,
567 making the fallout deposit entirely co-PDC in origin (Bonadonna et al., 2002; Engwell and Eychenne,
568 2016). The Vulcanian eruption produced both an eruptive column at the vent and PDCs on the
569 volcano's flank; the fallout deposit consequently includes ash from both vent-derived and co-PDC
570 plumes (Bonadonna et al., 2002). These two natural events, with distinct eruption characteristics,
571 allow us to demonstrate how our analysis techniques can be used on natural material to identify

572 secondary fragmentation. To compare with experimental samples, we analysed the componentry, AF
573 (Figure 9) and proportion of broken crystals in the 2 φ grain size fraction (Figure S2) of each sample.

574 The 2 φ fraction of both natural samples comprises approximately 30% dense material (crystals,
575 phenocrysts and vesicle-free glass). The Vulcanian sample however, contains 15% crystals with
576 adhered glass whereas the dome collapse sample contains approximately 20% (Figure 10). Hence the
577 Vulcanian sample comprises approximately 55% vesicular fragments, while the ash produced by
578 dome collapse contains less than 50%. Of this vesicular portion, the Vulcanian sample is comprised
579 mostly of microlite-free vesicular glass fragments. In comparison, the dome collapse sample is
580 comprised entirely of the microlite-rich vesicular glass. The higher proportion of vesicular microlite-
581 free glass in the Vulcanian sample indicates that in addition to microlite-bearing magma stored at
582 shallow levels (top of the conduit or dome), deep magma was erupted in the Vulcanian explosion. In
583 contrast, the dome collapse event involved only material previously extruded in the dome, comprising
584 microlite-rich glass of variable vesicularity. The two natural samples also differ in patterns of matrix
585 adherence. The AF distribution of the Vulcanian sample is trimodal, with a major mode at AF ~0.2
586 (low adhering matrix) and two minor modes at AF ~0.6 and 0.8 (Figs. 9 and S2). In comparison, the
587 dome collapse sample shows a uniform AF distribution (Figure 9) and a higher proportion of broken
588 crystals at low AF values (Figure S2).

589 Although this natural case study is illustrative only, and uses a single grain size fraction at a single
590 location for each eruption, both the components and the AF distributions are distinctive. The
591 differences in componentry (vesicle and microlite content) of the natural samples can be explained by
592 the fact that they experienced different ascent and fragmentation histories and different transportation
593 modes (PDCs vs. plumes); both of which should affect the mechanical properties. The Vulcanian
594 sample includes both particles transported directly in a plume and particles that were first transported
595 in PDCs before being entrained into co-PDC plumes. These two events can be observed, respectively,
596 in Figure 9 as a group of poorly abraded particles (high AF values) and a set of highly abraded
597 particles (low AF values). The dome collapse sample is dominated by microlite-rich particles that
598 were entirely transported in PDCs. The uniform AF distribution suggests that abrasion during

599 transport did not affect all the phenocrysts uniformly. Differences might reflect: (1) the robustness of
600 particles due to their high microlite content and moderate vesicularity compared to the highly
601 vesicular, microlite-free particles produced by the Vulcanian eruption; and/or (2) the coarser initial
602 grain size distribution in the dome collapse block-and-ash flows compared to the explosively
603 produced Vulcanian pumice flows, whereby larger initial particle sizes would require more abrasion
604 to release phenocrysts from the matrix. This points to a limitation of our analysis, which is that we
605 have not attempted to assess variations as a function of time/distance. At Tungurahua volcano, it has
606 been suggested that dense crystal-rich PDCs become increasingly crystal rich with time/distance as
607 the vesicular material is removed through abrasion (Douillet et al., 2013). This hypothesis could be
608 tested by applying our techniques to an appropriate selection of samples from a range of locations.

609

610 **6. Conclusions**

611 Three fragmentation methods (rapid decompression, impact and milling) have been explored to
612 constrain fragmentation associated with three different eruptive processes (Figure 11). Analysed
613 GSDs are fractal, which means that they can be characterised by the fractal dimension D. Our data
614 show that an initial GSD with $D \approx 2.1$ produced by rapid decompression can be altered by secondary
615 fragmentation processes that generate fine particles. Importantly, however, D values produced by
616 secondary processes in our experiments reach only ~2.7 (Fig. 8), which is far from D >3 observed in
617 many silicic eruptions (e.g., Kaminski and Jaupart, 1998; Rust and Cashman, 2011). We suggest that
618 the relatively low D values reflect the role of the groundmass crystal population, which prevents
619 extensive crushing and grain size reduction.

620

621 We support this hypothesis by analysis of particle shape (Fig. 4), componentry (Fig. 5) and adherence
622 factor (AF; Fig. 9). These data show that secondary fragmentation by either impact or milling
623 dramatically reduces the matrix component (Fig. 5b); ash generated by milling becomes increasingly
624 rounded (less elongate), and ash exteriors generated by impacts becomes increasingly smooth (Fig. 4).
625 Both milling and impact also remove adhering matrix from crystals (decrease AF), with milling the

most efficient at this process. Importantly, products of primary fragmentation retain much more adhering matrix than products of secondary fragmentation by either milling or impact (Fig. 9). Together these data provide guidelines for assessing primary vs. secondary contributions to the total grain size population within an eruptive deposit.

To further explore the role of crystals, we analysed the crystal content of volcanic ash derived from rapid decompression. Most crystals fracture along cleavage planes, leaving a smooth and clean breakage surface. During the evacuation of a crystal-rich magma body driven by rapid decompression, crystal fragmentation is inevitable and indeed characteristic of the associated tephra fallout. The proportion of free crystals depends on the grain size considered. X-Ray CT measurements combined with componentry allowed us to describe the shift in crystal size during fragmentation by rapid decompression. These data are important because the size fractions dominated by juvenile crystals show enhanced sedimentation because crystal densities exceed those of vesicular clasts. Thus we suggest that consideration of crystal sizes and proportions could improve settling calculations that inform hazard maps and dispersion models.

Finally we illustrate the application of our analysis techniques to two samples from Soufriere Hills Volcano, Montserrat: one dome collapse sample with co-PDC ash only, and one Vulcanian sample with contributions from both primary and co-PDC fragmentation. These samples are distinct in both their components and their grain characteristics, particularly AF. The Vulcanian sample is dominated by deep-derived microlite-poor and highly vesicular glass. Ash particles have polymodal AF distributions, with a dominant mode at low AF (little adhering glass) and two other modes at higher AF. We suggest that the high AF modes reflect primary fragmentation, while the low AF mode is the signature of co-PDC ash. The dome collapse sample, in contrast, is dominated by microlite-rich glass of variable vesicularity. In this sample, the AF distribution is approximately uniform, and most likely reflects the wide range of groundmass textures (both vesicularity and crystallinity). This latter observation brings up one further point, which is that both primary and secondary fragmentation processes are strongly dependent on the original magma components. As a result, a full understanding

654 of ash attributes produced by different mechanisms requires a systematic study using starting
655 materials with different bubble and crystal attributes.
656
657 **Acknowledgements**
658 We thank the Henry Mosely X-Ray Imaging Facility, University of Manchester for their support with
659 the XRCT. Klaus Mayer and Cristian Montanaro are thanked for their support with the shock tube
660 experiments. KVC acknowledges the support of the AXA Research Fund and a Royal Society
661 Research Merit Award. TJJ was partly supported by NERC studentship NE/L0025901.
662
663
664 **References:**
665
666 Alatorre-Ibargüengoitia, M. A., Scheu, B., Dingwell, D. B., Delgado-Granados, H., and Taddeucci, J.,
667 2010, Energy consumption by magmatic fragmentation and pyroclast ejection during
668 Vulcanian eruptions: Earth and Planetary Science Letters, v. 291, no. 1, p. 60-69.
669 Alfano, F., Bonadonna, C., Volentik, A. C., Connor, C. B., Watt, S. F., Pyle, D. M., and Connor, L. J.,
670 2011, Tephra stratigraphy and eruptive volume of the May, 2008, Chaitén eruption, Chile:
671 Bulletin of Volcanology, v. 73, no. 5, p. 613-630.
672 Alidibirov, M., and Dingwell, D. B., 2000, Three fragmentation mechanisms for highly viscous magma
673 under rapid decompression: Journal of Volcanology and Geothermal Research, v. 100, no. 1–
674 4, p. 413-421.
675 Bachmann, O., Dungan, M. A., and Lipman, P. W., 2002, The Fish Canyon magma body, San Juan
676 volcanic field, Colorado: rejuvenation and eruption of an upper-crustal batholith: Journal of
677 Petrology, v. 43, no. 8, p. 1469-1503.
678 Best, M. G., and Christiansen, E. H., 1997, Origin of broken phenocrysts in ash-flow tuffs: Geological
679 Society of America Bulletin, v. 109, no. 1, p. 63-73.
680 Bindeman, I. N., 2005, Fragmentation phenomena in populations of magmatic crystals: American
681 Mineralogist, v. 90, no. 11-12, p. 1801-1815.
682 Bonadonna, C., Connor, L. J., Connor, C. B., and Courtland, L. M., 2010, Tephra2.
683 Bonadonna, C., Mayberry, G., Calder, E., Sparks, R., Choux, C., Jackson, P., Lejeune, A., Loughlin, S.,
684 Norton, G., and Rose, W., 2002, Tephra fallout in the eruption of Soufrière Hills Volcano,
685 Montserrat: Geological Society, London, Memoirs, v. 21, no. 1, p. 483-516.
686 Borg, I. Y., and Heard, H. C., 1970, Experimental Deformation Of Plagioclases, *in* Paulitsch, P., ed.,
687 Experimental and Natural Rock Deformation / Experimentelle und natürliche
688 Gesteinsverformung, Springer Berlin Heidelberg, p. 375-403.
689 Brown, W. L., and Macaudiére, J., 1984, Microfracturing in relation to atomic structure of plagioclase
690 from a deformed meta-anorthosite: Journal of Structural Geology, v. 6, no. 5, p. 579-586.
691 Cagnoli, B., and Manga, M., 2004, Granular mass flows and Coulomb's friction in shear cell
692 experiments: Implications for geophysical flows: Journal of Geophysical Research: Earth
693 Surface (2003–2012), v. 109, no. F4.
694 Carter, N. L., Officer, C. B., Chesner, C. A., and Rose, W. I., 1986, Dynamic deformation of volcanic
695 ejecta from the Toba caldera: Possible relevance to Cretaceous/Tertiary boundary
696 phenomena: Geology, v. 14, no. 5, p. 380-383.

697 Chouet, B. A., Page, R. A., Stephens, C. D., Lahr, J. C., and Power, J. A., 1994, Precursory swarms of
698 long-period events at Redoubt Volcano (1989–1990), Alaska: Their origin and use as a
699 forecasting tool: Journal of Volcanology and Geothermal Research, v. 62, no. 1–4, p. 95-135.
700 Cnudde, V., Masschaele, B., Dierick, M., Vlassenbroeck, J., Hoorebeke, L. V., and Jacobs, P., 2006,
701 Recent progress in X-ray CT as a geosciences tool: Applied Geochemistry, v. 21, no. 5, p. 826-
702 832.
703 Cordonnier, B., Hess, K. U., Lavallee, Y., and Dingwell, D. B., 2009, Rheological properties of dome
704 lavas: Case study of Unzen volcano: Earth and Planetary Science Letters, v. 279, no. 3–4, p.
705 263-272.
706 Dartevelle, S., Ernst, G. G., Stix, J., and Bernard, A., 2002, Origin of the Mount Pinatubo climactic
707 eruption cloud: Implications for volcanic hazards and atmospheric impacts: Geology, v. 30,
708 no. 7, p. 663-666.
709 Douillet, G. A., Tsang-Hin-Sun, È., Kueppers, U., Letort, J., Pacheco, D. A., Goldstein, F., Von Aulock,
710 F., Lavallée, Y., Hanson, J. B., and Bustillos, J., 2013, Sedimentology and geomorphology of
711 the deposits from the August 2006 pyroclastic density currents at Tungurahua volcano,
712 Ecuador: Bulletin of Volcanology, v. 75, no. 11, p. 1-21.
713 Dufek, J., and Manga, M., 2008, In situ production of ash in pyroclastic flows: Journal of Geophysical
714 Research: Solid Earth, v. 113, no. B9.
715 Elangovan, P., Hezel, D. C., Howard, L., Armstrong, R., and Abel, R. L., 2012, PhaseQuant: A tool for
716 quantifying tomographic data sets of geological specimens: Computers & Geosciences, v. 48,
717 no. 0, p. 323-329.
718 Engwell, S., Sparks, R., and Carey, S., 2014, Physical characteristics of tephra layers in the deep sea
719 realm: the Campanian Ignimbrite eruption: Geological Society, London, Special Publications,
720 v. 398, no. 1, p. 47-64.
721 Engwell, S., **Eychenne, J., 2016.** Chapter 4: Contribution of fine ash to the atmosphere from
722 plumes associated with pyroclastic density currents. In *Volcanic Ash: Hazard Observation*, edited
723 by Mackie, S., Ricketts, H., Watson, M., Cashman, K., Rust, A. *Elsevier. 67-85pp.*
724 Eychenne, J., Cashman, K., Rust, A., and Durant, A., 2015, Impact of the lateral blast on the spatial
725 pattern and grain size characteristics of the 18 May 1980 Mount St. Helens fallout deposit:
726 Journal of Geophysical Research: Solid Earth, v. 120, no. 9, p. 6018-6038.
727 Eychenne, J., Le Pennec, J.-L., Troncoso, L., Gouhier, M., and Nedelec, J.-M., 2012, Causes and
728 consequences of bimodal grain-size distribution of tephra fall deposited during the August
729 2006 Tungurahua eruption (Ecuador): Bulletin of volcanology, v. 74, no. 1, p. 187-205.
730 Félix, G., and Thomas, N., 2004, Relation between dry granular flow regimes and morphology of
731 deposits: formation of levées in pyroclastic deposits: Earth and Planetary Science Letters, v.
732 221, no. 1, p. 197-213.
733 Freundt, A., and Schmincke, H.-U., 1992, Abrasion in pyroclastic flows: Geologische Rundschau, v. 81,
734 no. 2, p. 383-389.
735 Genareau, K., Proussevitch, A. A., Durant, A. J., Mulukutla, G., and Sahagian, D. L., 2012, Sizing up the
736 bubbles that produce very fine ash during explosive volcanic eruptions: Geophysical
737 Research Letters, v. 39, no. 15.
738 Hartmann, W. K., 1969, Terrestrial, lunar, and interplanetary rock fragmentation: Icarus, v. 10, no. 2,
739 p. 201-213.
740 Hull, D., 1999, Fractography: observing, measuring and interpreting fracture surface topography,
741 Cambridge University Press.
742 Jones, T., Wadsworth, F., Vasseur, J., Lavallee, Y., Hess, K., Scheu, B., and Dingwell, D., Porosity and
743 Textural Evolution of Bubbly Magma under High-Temperature Uniaxial Deformation, *in*
744 Proceedings AGU Fall Meeting Abstracts2013, Volume 1, p. 2715.
745 Kaminski, E., and Jaupart, C., 1998, The size distribution of pyroclasts and the fragmentation
746 sequence in explosive volcanic eruptions: Journal of Geophysical Research: Solid Earth, v.
747 103, no. B12, p. 29759-29779.

748 Kelly, A., and Macmillan, N. H., 1986, Strong solids, Clarendon Press Oxford.
749 Kennedy, B., Spieler, O., Scheu, B., Kueppers, U., Taddeucci, J., and Dingwell, D. B., 2005, Conduit
750 implosion during Vulcanian eruptions: Geology, v. 33, no. 7, p. 581-584.
751 Korvin, G., 1992, Fractal models in the earth sciences, Elsevier Science Ltd.
752 Kueppers, U., Perugini, D., and Dingwell, D. B., 2006a, "Explosive energy" during volcanic eruptions
753 from fractal analysis of pyroclasts: Earth and Planetary Science Letters, v. 248, no. 3, p. 800-
754 807.
755 Kueppers, U., Putz, C., Spieler, O., and Dingwell, D. B., 2012, Abrasion in pyroclastic density currents:
756 insights from tumbling experiments: Physics and Chemistry of the Earth, Parts A/B/C, v. 45,
757 p. 33-39.
758 Kueppers, U., Scheu, B., Spieler, O., and Dingwell, D. B., 2006b, Fragmentation efficiency of explosive
759 volcanic eruptions: a study of experimentally generated pyroclasts: Journal of Volcanology
760 and Geothermal Research, v. 153, no. 1, p. 125-135.
761 Liu, E., Cashman, K., Rust, A., and Gislason, S., 2015a, The role of bubbles in generating fine ash
762 during hydromagmatic eruptions: Geology, v. 43, no. 3, p. 239-242.
763 Liu, E. J., Cashman, K. V., and Rust, A. C., 2015b, Optimising shape analysis to quantify volcanic ash
764 morphology: GeoResJ, v. 8, p. 14-30.
765 Manga, M., Patel, A., and Dufek, J., 2011, Rounding of pumice clasts during transport: field
766 measurements and laboratory studies: Bulletin of Volcanology, v. 73, no. 3, p. 321-333.
767 Martel, C., Dingwell, D. B., Spieler, O., Pichavant, M., and Wilke, M., 2001, Experimental
768 fragmentation of crystal-and vesicle-bearing silicic melts: Bulletin of volcanology, v. 63, no. 6,
769 p. 398-405.
770 Meyer, J., 1971, Glass crust on intratelluric phenocrysts in volcanic ash as a measure of eruptive
771 violence: Bulletin Volcanologique, v. 35, no. 2, p. 358-368.
772 Miwa, T., and Geshi, N., 2012, Decompression rate of magma at fragmentation: Inference from
773 broken crystals in pumice of vulcanian eruption: Journal of Volcanology and Geothermal
774 Research, v. 227, p. 76-84.
775 Mueller, S. B., Lane, S. J., and Kueppers, U., 2015, Lab-scale ash production by abrasion and collision
776 experiments of porous volcanic samples: Journal of Volcanology and Geothermal Research,
777 v. 302, p. 163-172.
778 Pallister, J. S., Hoblitt, R. P., Meeker, G. P., Knight, R. J., and Siems, D. F., 1996, Magma mixing at
779 Mount Pinatubo: petrographic and chemical evidence from the 1991 deposits: Fire and Mud:
780 Eruptions and Lahars of Mount Pinatubo, Philippines. Quezon City: Philippine Institute of
781 Volcanology and Seismology, p. 687-731.
782 Perugini, D., and Kueppers, U., 2012, Fractal analysis of experimentally generated pyroclasts: A tool
783 for volcanic hazard assessment: Acta Geophysica, v. 60, no. 3, p. 682-698.
784 Perugini, D., Speziali, A., Caricchi, L., and Kueppers, U., 2011, Application of fractal fragmentation
785 theory to natural pyroclastic deposits: Insights into volcanic explosivity of the Valentano
786 scoria cone (Italy): Journal of Volcanology and Geothermal Research, v. 202, no. 3, p. 200-
787 210.
788 Rose, W., and Durant, A., 2009, Fine ash content of explosive eruptions: Journal of Volcanology and
789 Geothermal Research, v. 186, no. 1, p. 32-39.
790 Rust, A., and Cashman, K., 2011, Permeability controls on expansion and size distributions of
791 pyroclasts: Journal of Geophysical Research: Solid Earth, v. 116, no. B11.
792 Scheu, B., Kueppers, U., Mueller, S., Spieler, O., and Dingwell, D. B., 2008, Experimental volcanology
793 on eruptive products of Unzen volcano: Journal of Volcanology and Geothermal Research, v.
794 175, no. 1–2, p. 110-119.
795 Sparks, R., and Walker, G., 1977, The significance of vitric-enriched air-fall ashes associated with
796 crystal-enriched ignimbrites: Journal of Volcanology and Geothermal Research, v. 2, no. 4, p.
797 329-341.

798 Spieler, O., Kennedy, B., Kueppers, U., Dingwell, D. B., Scheu, B., and Taddeucci, J., 2004, The
799 fragmentation threshold of pyroclastic rocks: Earth and Planetary Science Letters, v. 226, no.
800 1–2, p. 139-148.
801 Taddeucci, J., Pompilio, M., and Scarlato, P., 2004, Conduit processes during the July–August 2001
802 explosive activity of Mt. Etna (Italy): inferences from glass chemistry and crystal size
803 distribution of ash particles: Journal of Volcanology and Geothermal Research, v. 137, no. 1,
804 p. 33-54.
805 Tait, S., 1992, Selective preservation of melt inclusions in igneous phenocrysts: American
806 Mineralogist, v. 77, no. 1-2, p. 146-155.
807 Turcotte, D., 1986, Fractals and fragmentation: Journal of Geophysical Research: Solid Earth (1978–
808 2012), v. 91, no. B2, p. 1921-1926.
809 Walker, G. P., 1973, Explosive volcanic eruptions—a new classification scheme: Geologische
810 Rundschau, v. 62, no. 2, p. 431-446.
811 Williamson, B., Di Muro, A., Horwell, C., Spieler, O., and Llewellin, E., 2010, Injection of vesicular
812 magma into an andesitic dome at the effusive–explosive transition: Earth and Planetary
813 Science Letters, v. 295, no. 1, p. 83-90.
814 Zhang, Y., 1998, Mechanical and phase equilibria in inclusion-host systems: Earth and Planetary
815 Science Letters, v. 157, no. 3-4, p. 209-222.
816 Zimanowski, B., Wohletz, K., Dellino, P., and Büttner, R., 2003, The volcanic ash problem: Journal of
817 Volcanology and Geothermal Research, v. 122, no. 1, p. 1-5.

818

Figure Captions:

Figure 1: 3D surface reconstructions of the crystal phases. Processed using Avizo software from X-Ray computed tomography generated image stacks. **(a)** SHV subvolume. **(b)** Cumulative frequency diagram showing the relative crystal volume distributions within SHV pumice extracted from 3D reconstructions.

Figure 2: Diagrams of the various fragmentation apparatus used in this study. **(a)** shock tube (modified after Alatorre-Ibargüengoitia et al. (2010)) , **(b)** falling piston and **(c)** ball mill.

Figure 3: Grain size distributions for **(a)** rapid decompression shock tube, **(b)** falling piston and **(c)** ball mill experiments.

Figure 4: Shape analysis from BSE SEM images of 2φ grain size fraction. Histograms show shape data gathered from 2D SEM image mosaics. Where an axial ratio of one implies a perfectly round grain and a convexity of one implies a smooth grain with the same perimeter as its convex hull. **(a)** The difference in axial ratio of the grains produced by hot and cold decompression. **(b)** The change in the axial ratio value for grains that were hit 5 and 10 times. **(c)** The change in the axial ratio value for grains that were milled for 30 seconds and one minute. **(d)** The difference in convexity values of the grains produced by hot and cold decompression. **(e)** The change in value of convexity in grains hit 5 and 10 times. **(f)** The change in the value of convexity for grains that were milled for 30 seconds and one minute.

Figure 5: Componentry results for experimentally generated ash. **(a)** SHV average componentry results from rapid decompression, normalised per grain size fraction. **(b)** Individual ash grain componentry from the 2φ grain size fraction using BSE SEM images of products of varying fragmentation techniques.

847 **Figure 6**: Normalised crystal distributions for SHV represented as a cumulative distribution. Solid
848 lines represent the crystal population present in the volcanic core prior to experimental fragmentation.
849 Dashed lines represent the experimentally fragmented crystal population.
850
851 **Figure 7:** SEM micrographs of crystals from the SHV 2φ ash fraction. **(a)** Hornblende crystal
852 showing mainly a clean flat surface however extremely irregular at the edges. **(b)** Broken crystal with
853 a thin vesicular glass coating. **(c)** Hornblende crystal with a stepped fracture surface. **(d)** A plagioclase
854 crystal showing multiple river line fractures on broken crystal surface.
855
856 **Figure 8:** Power law plots for **(a)** the rapid decompression experiments, **(b)** the falling piston
857 experiments and **(c)** the ball mill experiments. Data markers represent those included in the linear
858 regression.
859
860 **Figure 9:** Adherence Factor plot of the three fragmentation techniques: Milling (0.5 minutes and 1
861 minute), Impact (5 hits and 10 hits) rapid decompression (cold and hot) and natural samples
862 (Vulcanian and dome collapse). Adherence Factor (AF) = area of matrix / (area of matrix + area of
863 crystal) against the total cumulative per cent. A high value for AF represents a higher proportion of
864 adhered matrix and thus the upper curve shows a greater amount of 'matrix stripping' than the lower
865 curve. Normalised Grain No. is the value of AF in descending order, normalised to one.
866
867 **Figure 10:** Componentry of two natural SHV samples. The samples are from fallout deposits
868 produced by a dome collapse event (on 31 March 1997) and a Vulcanian eruption (on 26 September
869 1997) of Soufriere Hills Volcano.
870
871 **Figure 11:** A summary cartoon relating the three experimental fragmentation mechanism to the
872 natural volcanic scenario. Primary fragmentation through rapid decompression produces pyroclasts

873 with D ~2.2. Then through abrasion and milling, selective secondary fragmentation increases D and
874 adds to the fine ash component to the GSD.
875
876 **Table 1:** Summary of all experimental runs and characterisation. Grey fields indicate that the
877 characterisation has been performed.
878
879 **Table 2:** A review of relevant fragmented material and the associated fractal dimensions obtained.
880
881 **Figure S1:** Individual power-law plots for each experimental fragmentation experiment: **(a)** rapid
882 decompression **(b)** impact and **(c)** milling. Open circles represent the data points not included in the
883 linear fitting.
884
885 **Figure S2:** Histogram of adherence factor values for decompression (hot and cold), impact (5 hits and
886 10 hits), milling (30 seconds and 1 minute) and natural samples (Vulcanian and dome collapse).
887 Shown on bars is the proportion of broken crystals amongst the crystal population where a broken
888 crystal is defined as a crystal that clearly does not display an intact ring of zoning.
889
890

Table 1

Click here to download Table: Table_1_exp_conditions.docx

Fragmentation Mechanism	Experimental conditions	Pre-fragmentation characterisation					Post-fragmentation characterisation						
		Representative thin section	Representative XRCT scan	Connected porosity (%)	Isolated porosity (%)	Total porosity (%)	GSD	Fractals	Course Componentry	Fine (Ash) Componentry	Shape Analysis	Crystal volume shift	SEM imagery of fractures
Rapid Decompression	**20°C, 15MPa**			64.62	1.52	66.14							
	20°C, 30MPa			65.31	1.72	67.03							
	880°C, 15MPa			63.60	2.18	65.78							
	880°C, 30MPa			64.15	1.74	65.89							
Impact	**5 Hits**												
	10 Hits												
	15 Hits												
	20 Hits												
	25 Hits												
Milling	**0.5 min**												
	1 min												
	2.5 mins												
	5 mins												

Table 1: Jones et al (2016, JVGR)

Table 2
Click here to download Table: Table_2_fractal_review.docx

Material	Natural (N)/ Experimental (E)	D	Reference:
Mt Unzen 1992-95, 7% ϕ_c	E	2.1	(Kueppers et al., 2006)
Mt Unzen 1992-95, 20.5% ϕ_c	E	2.3	(Kueppers et al., 2006)
Mt Unzen 1992-95, 35.5% ϕ_c	E	2.5	(Kueppers et al., 2006)
SHV (Rapid Decompression)	E	2.1*	This study
SHV (Impact)	E	2.6*	This study
SHV (Milling)	E	2.4*	This study
Falling Piston	E	2.6	(Kaminski and Jaupart, 1998)
Ball milling (without balls)	E	4.2	(Kaminski and Jaupart, 1998)
Ball milling (with balls)	E	5.4	(Kaminski and Jaupart, 1998)
Mt. Spurr August 1992	N (Total GSD)	3.0	(Durant and Rose, 2009)
Askja D, Iceland 1875	N (Fall)	3.0	(Sparks et al., 1981)
MSH, May 18, 1980 Plinian	N (Total GSD)	3.2	(Carey and Sigurdsson, 1982)
Mt. Spurr September 1992	N (Total GSD)	3.2	(Durant and Rose, 2009)
Hudson, Chille	N (Fall)	3.3	(Scasso et al., 1994)
Fogo A, Azores	N (Fall)	3.3	(Bursik et al., 1992)
Hachinohe, Japan	N (Fall)	3.5	(Hayakawa, 1985)
Krakatau, Indonesia	N (PDC)	3.3	(Carey et al., 1996)
Taupo, New Zealand	N (PDC)	3.3	(Walker and Wilson, 1983)
Fuego	N (Fall)	2.1	(Rust and Cashman, 2011)
Quizapu	N (Total GSD)	3.2	(Rust and Cashman, 2011)
Heimaey	N (Fall)	2.1	(Rust and Cashman, 2011)
El Chichon 1 and 3	N (Total GSD)	3.1	(Rust and Cashman, 2011)

* Mean average D for that fragmentation mechanism. D reported to 1 d.p.

Table 2: Jones et al (2016, JVGR)

All figures

Click here to download Figure: JONES_FINAL_ALL_FIGS.pdf

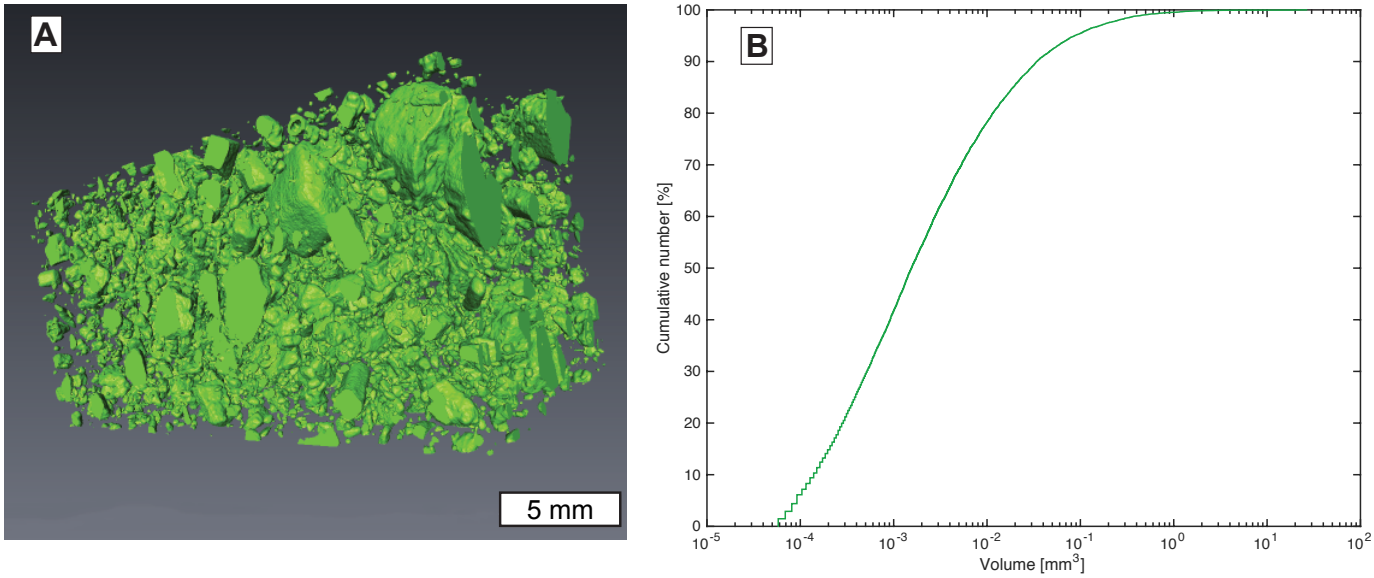

Figure 1: Jones et al (2016, JVGR)
Size: 1.5 column

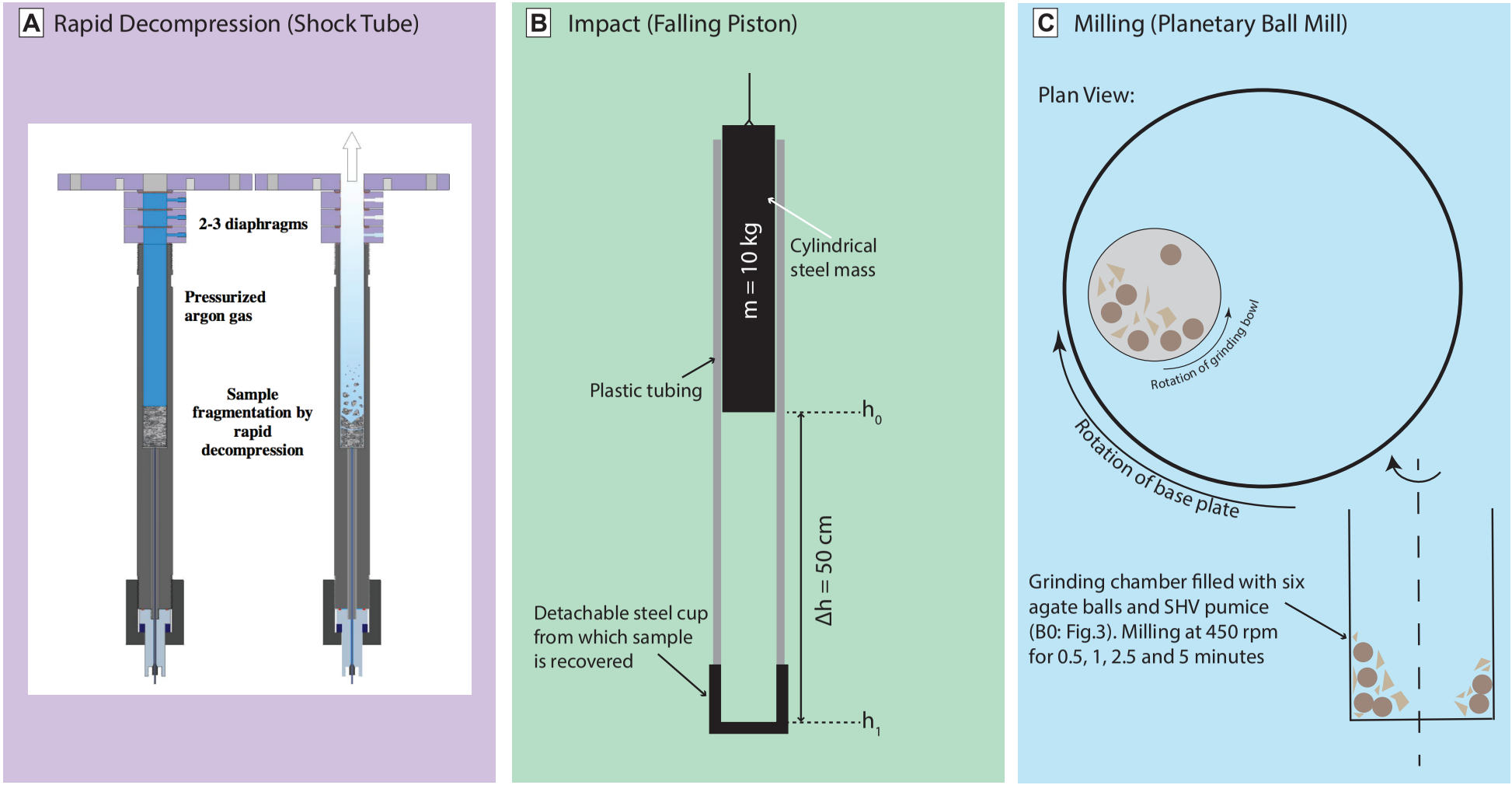

Figure 2: Jones et al. (2016, JVGR)
Size: Double column

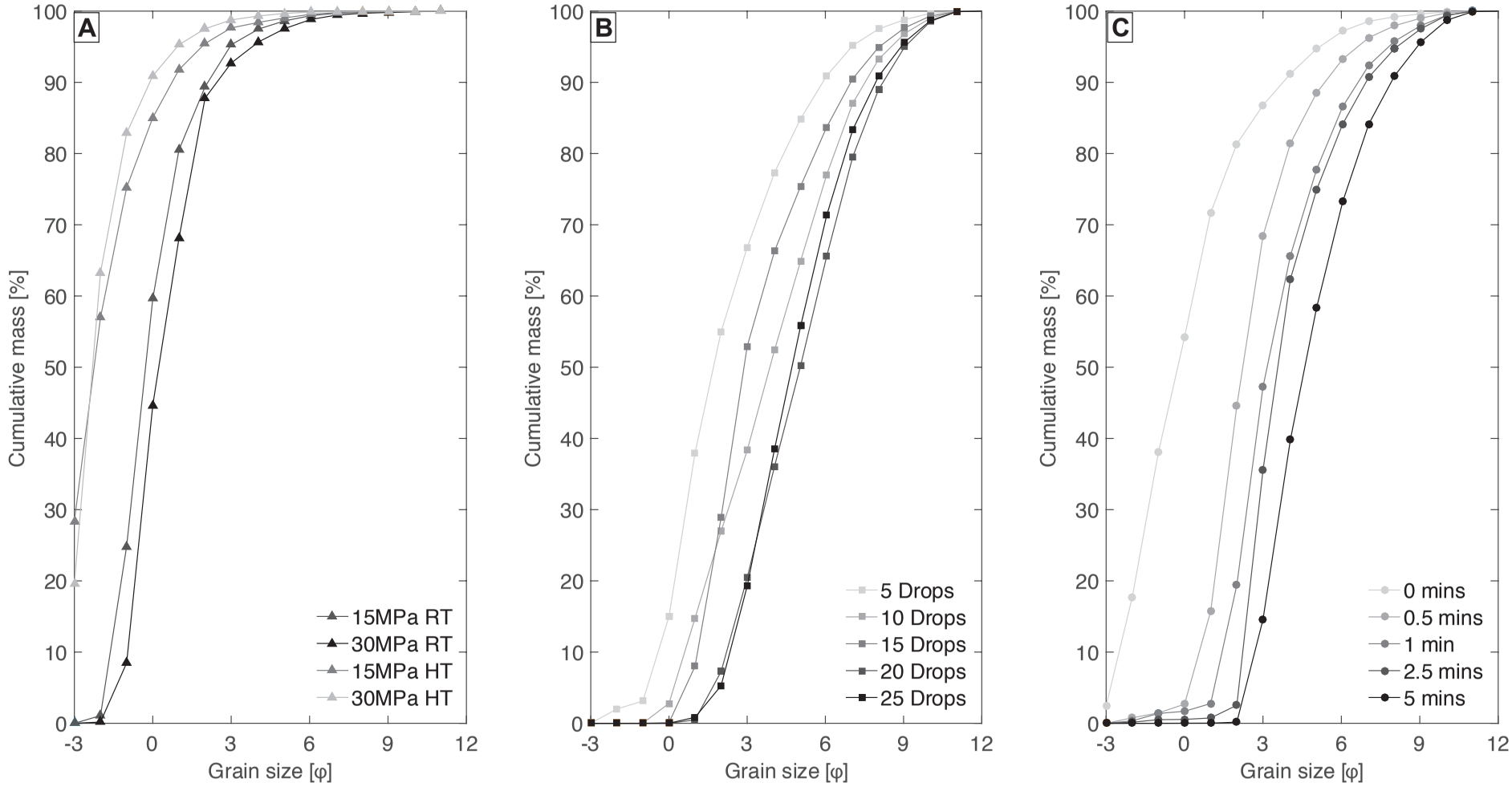

Figure 3: Jones et al. (2016, JVGR)
Size: Double column

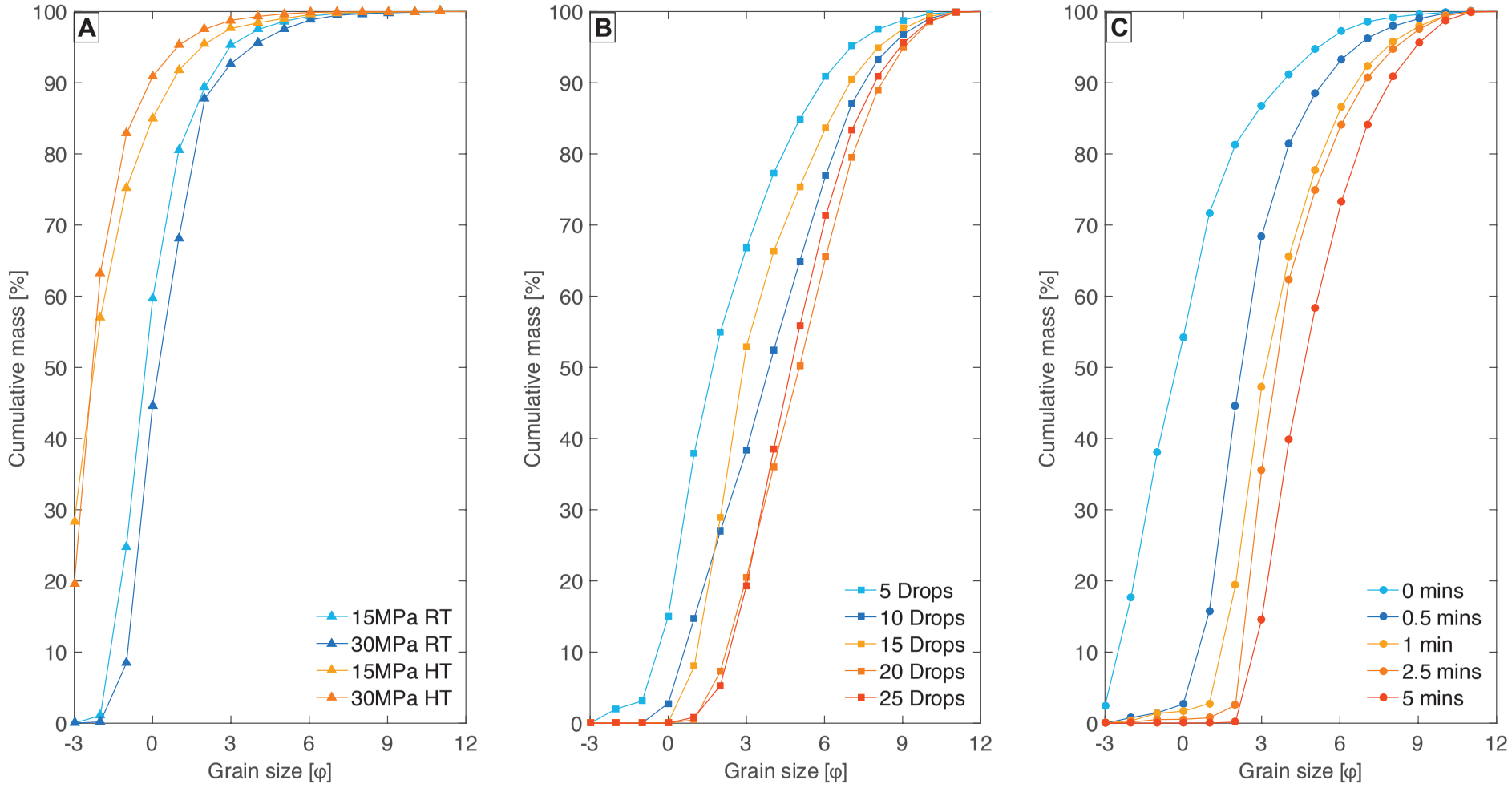

Figure 3: Jones et al. (2016, JVGR)
Size: Double column

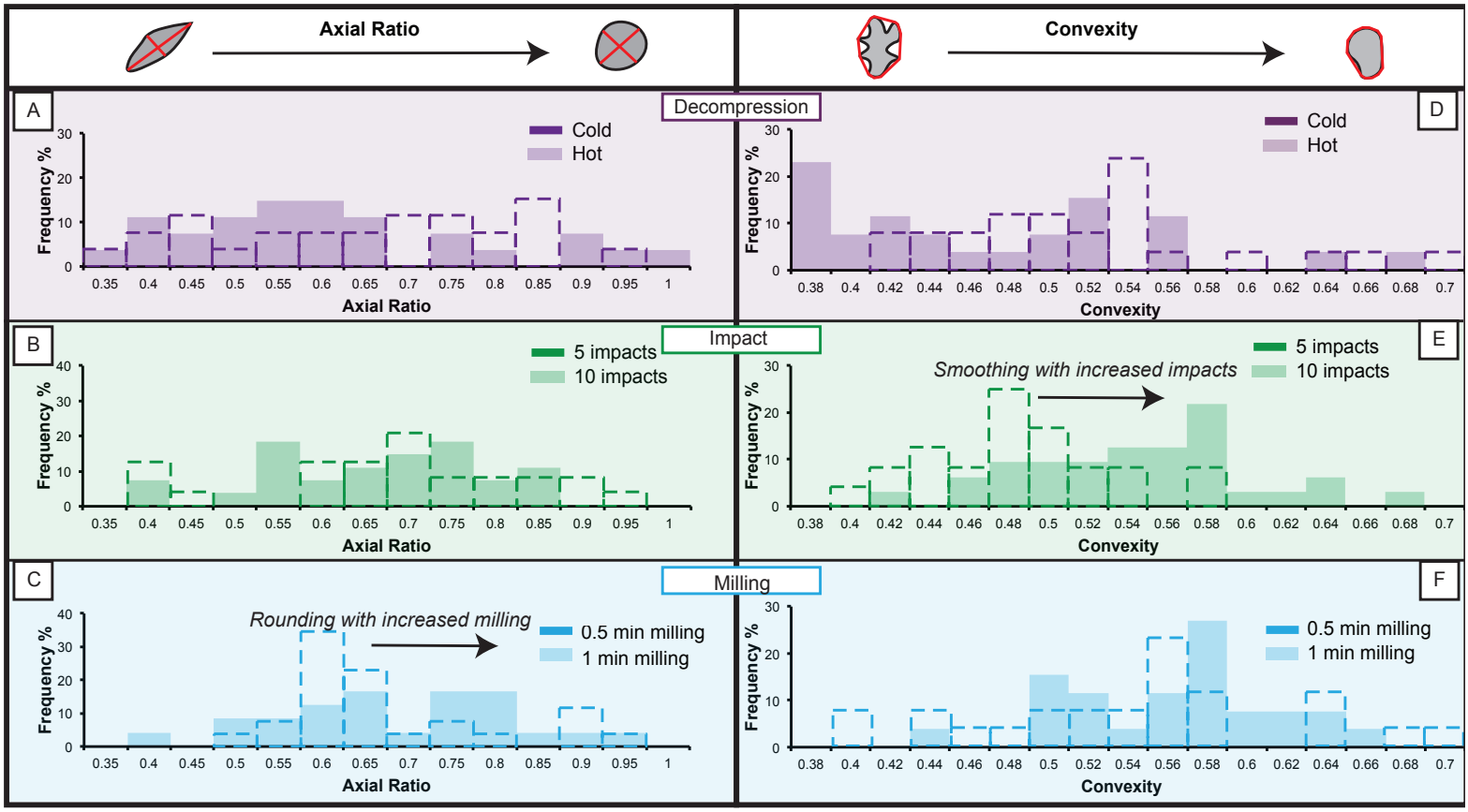

Figure 4: Jones et al. (2016, JGVR)
Size: 2 column

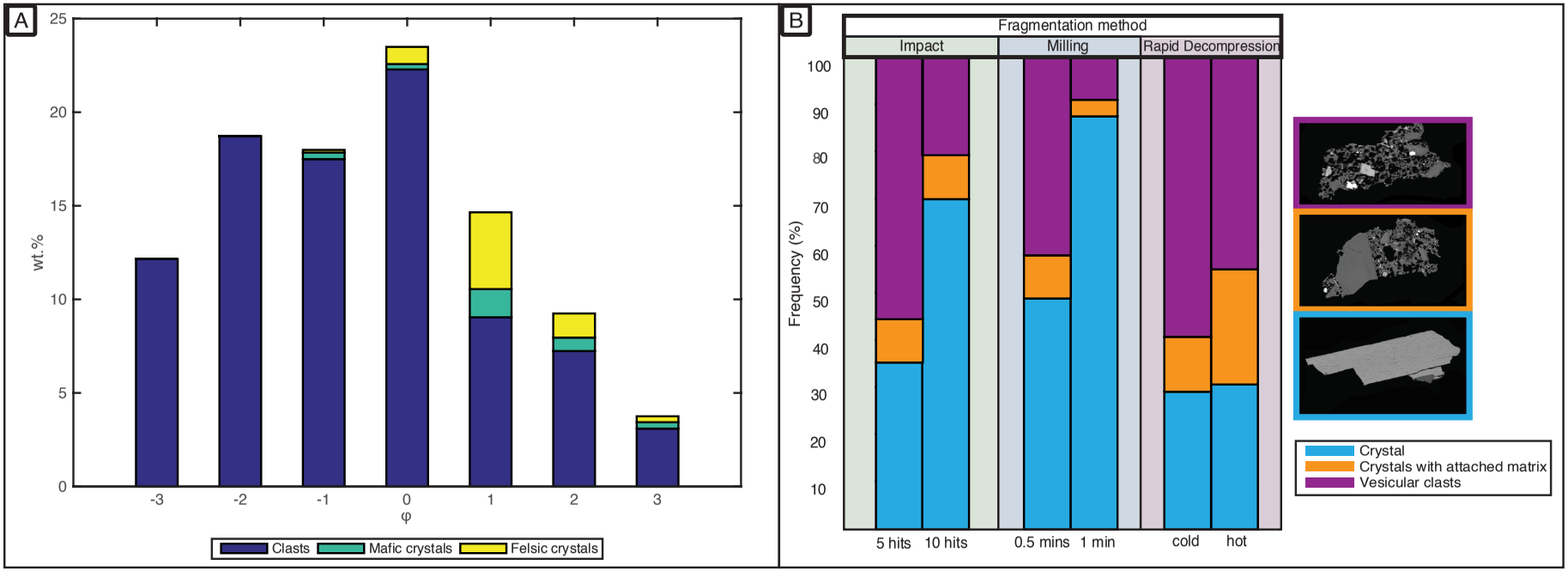

Figure 5: Jones et al (2016, JVGR)
Size: Double Collumn

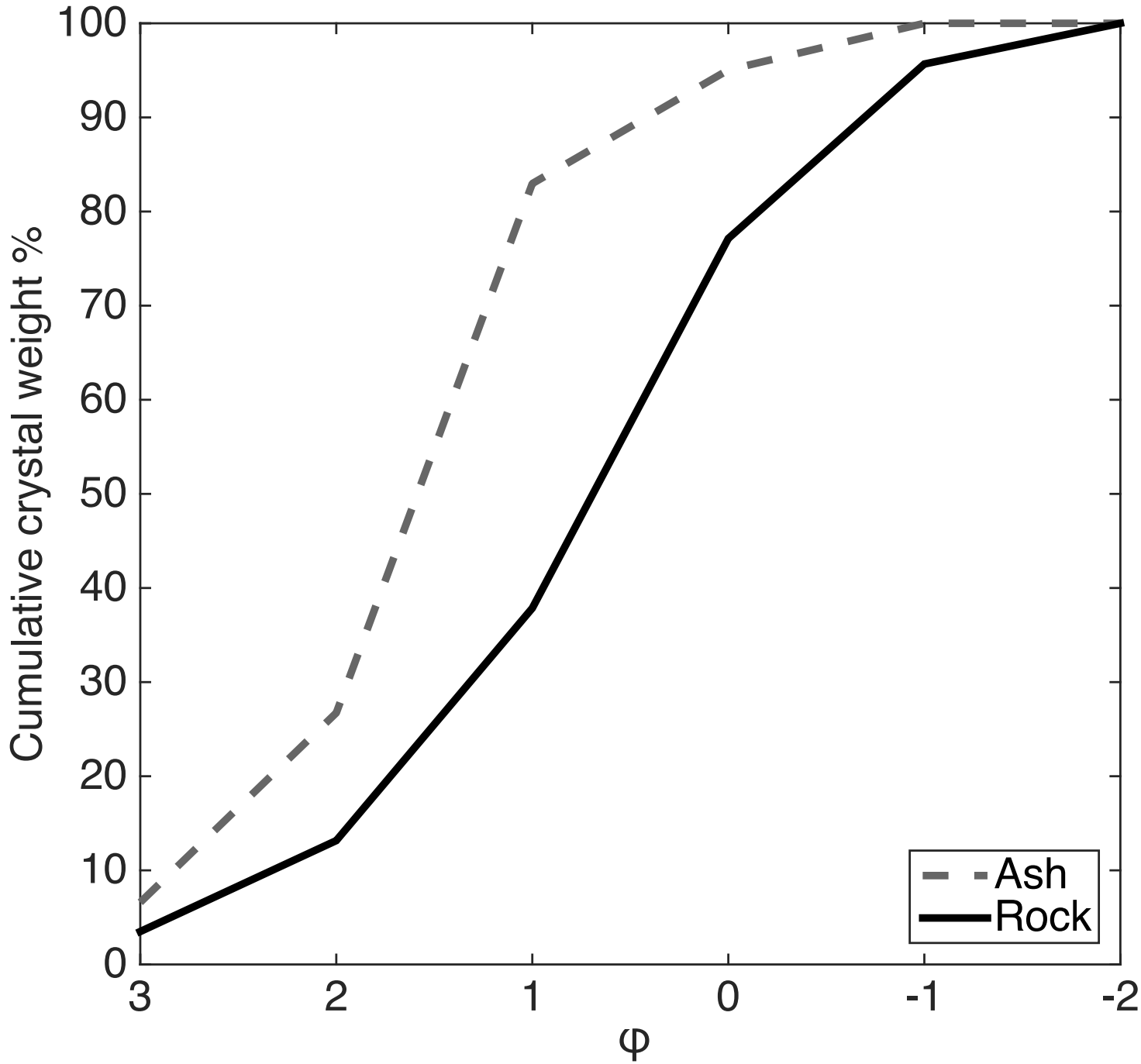

Figure 6: Jones et al. (2016, JVGR) Size: Single Column

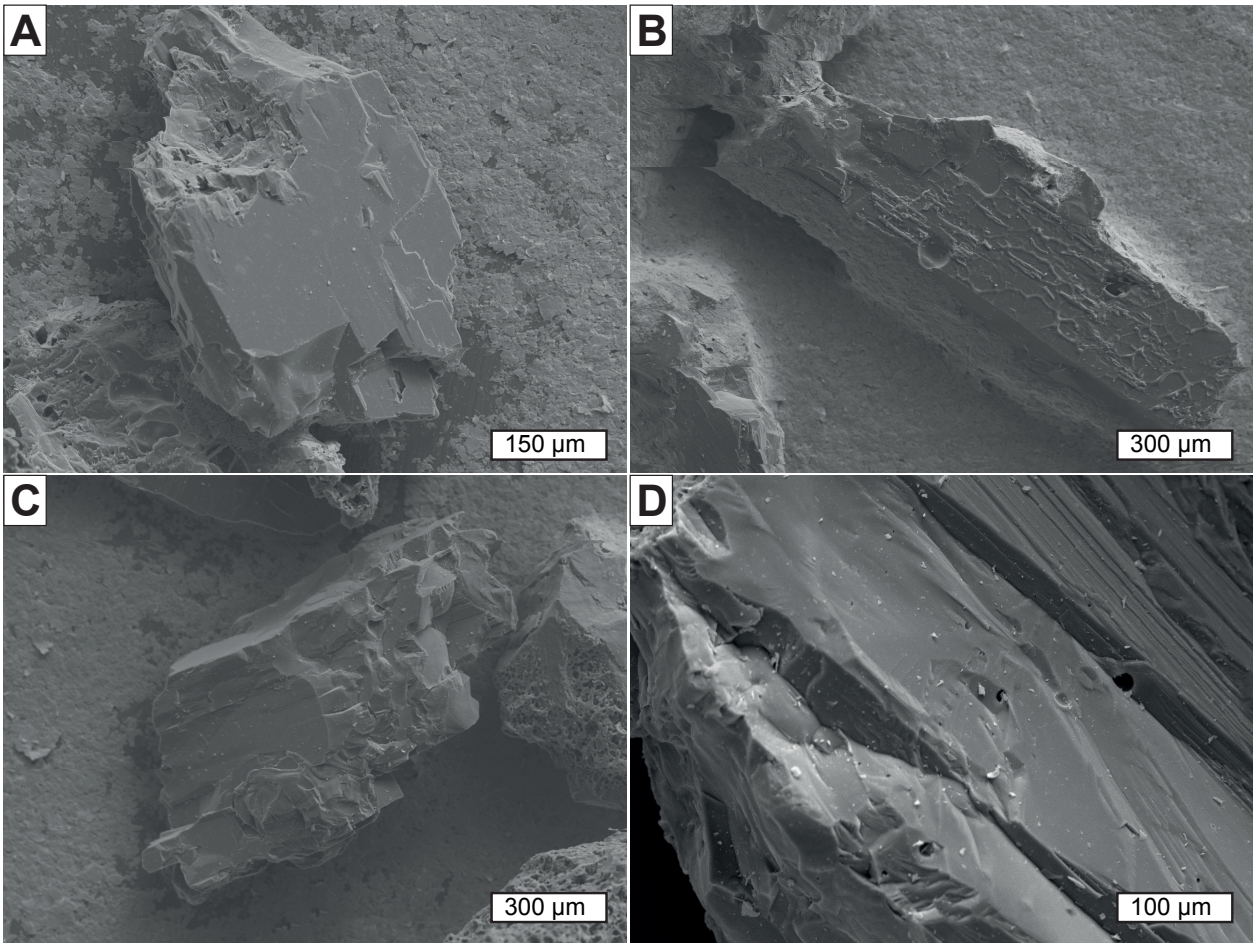

Figure 7: Jones et al (2016, JVGR)
Size: Single column

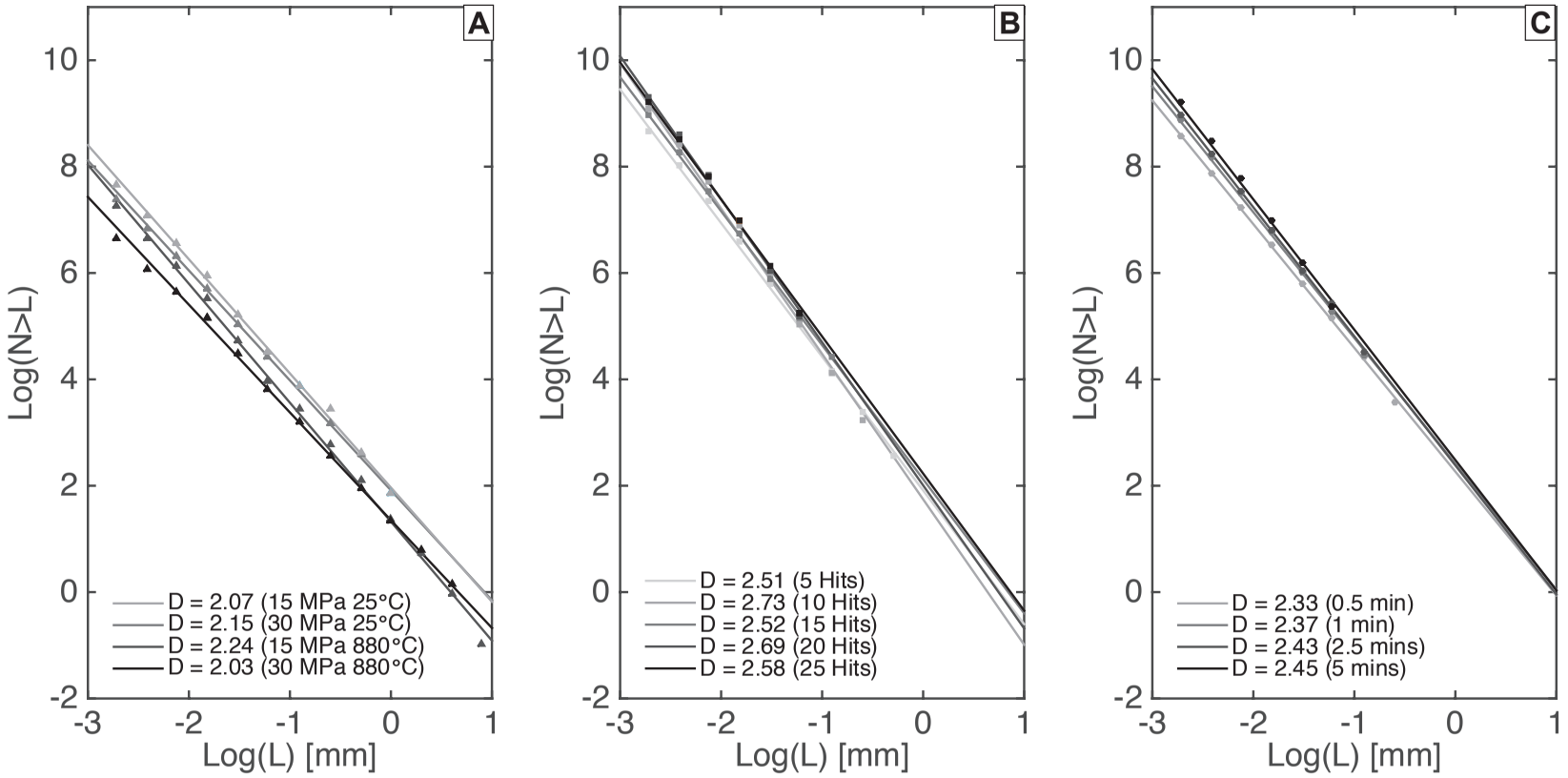

Figure 8: Jones et al. (2016, JVGR)
Size: Double column

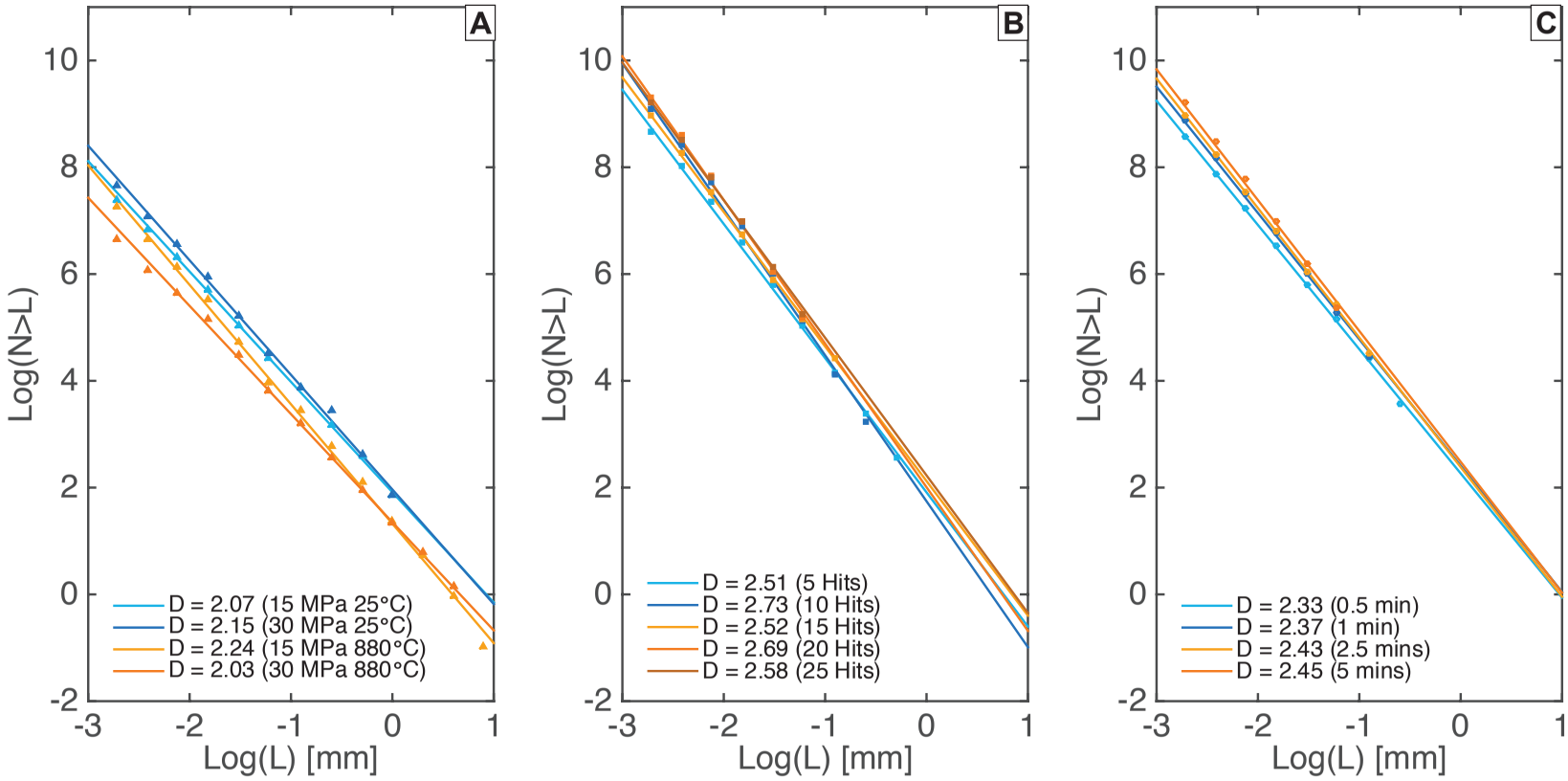

Figure 8: Jones et al. (2016, JVGR)
Size: Double column

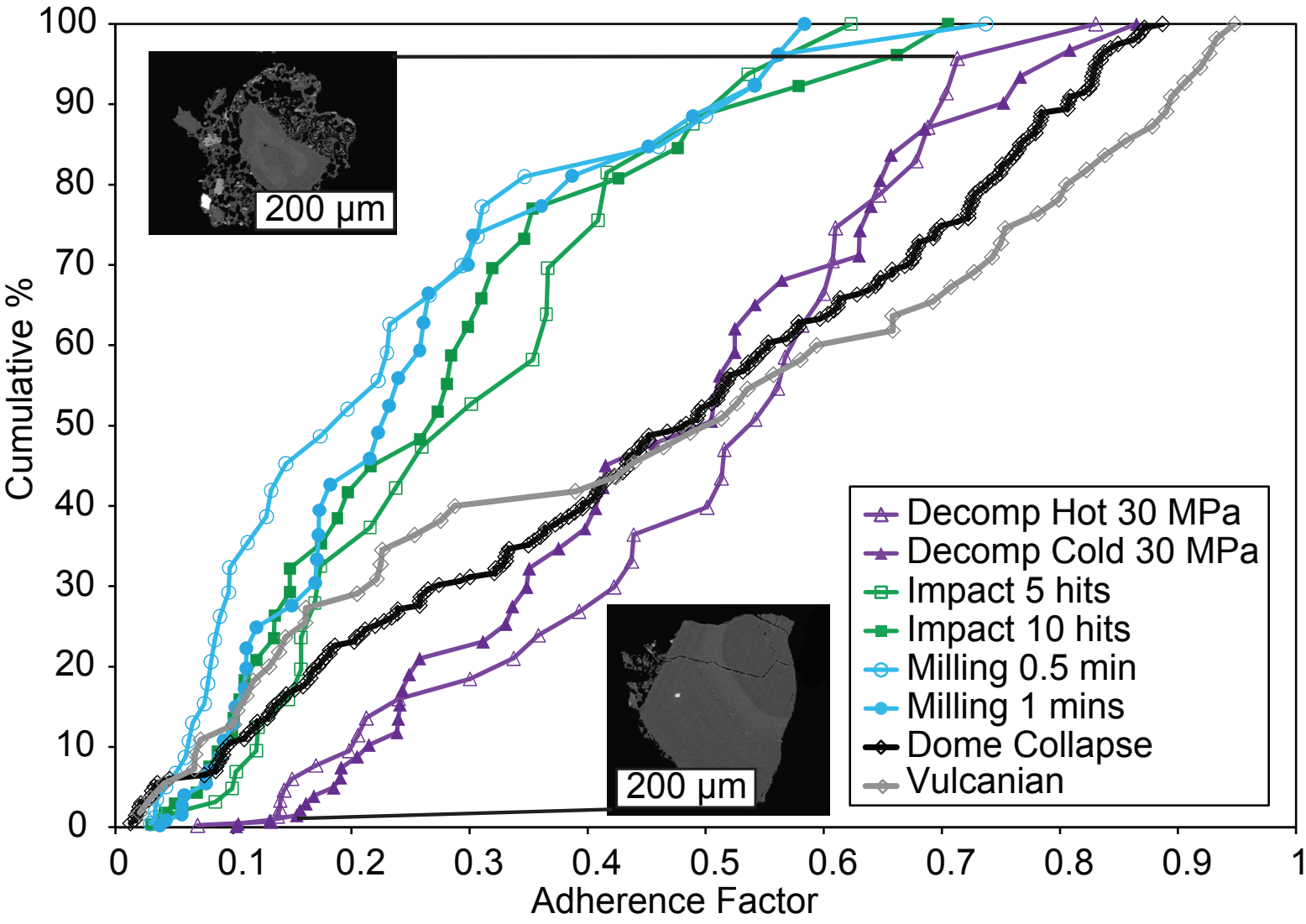

Figure 9: Jones et al. (2016, JGVR)
Size: Single column

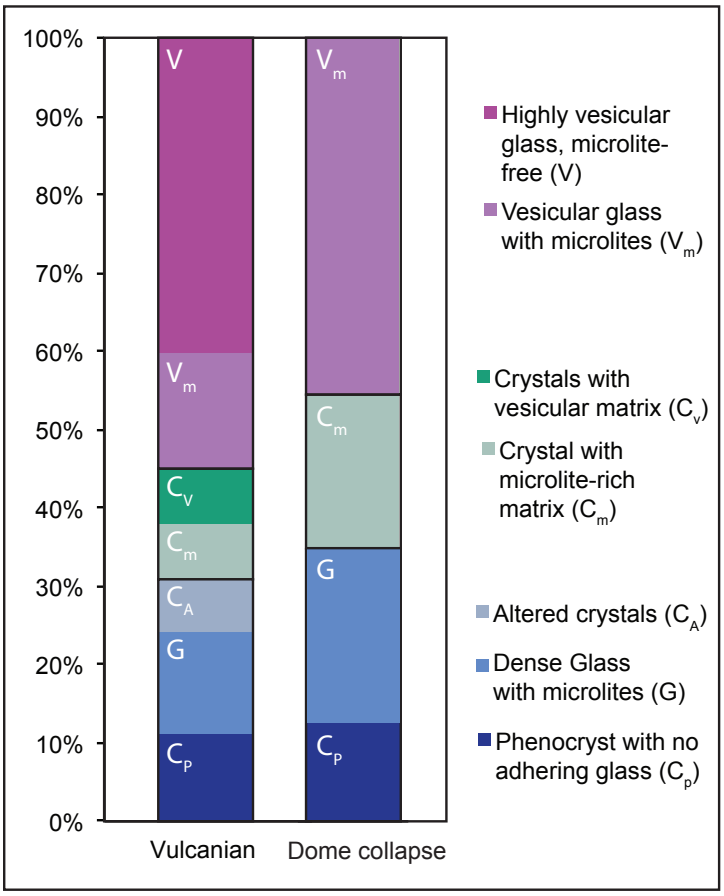

Figure 10: Jones et al. (2016, JVGR)
Size: Single Column

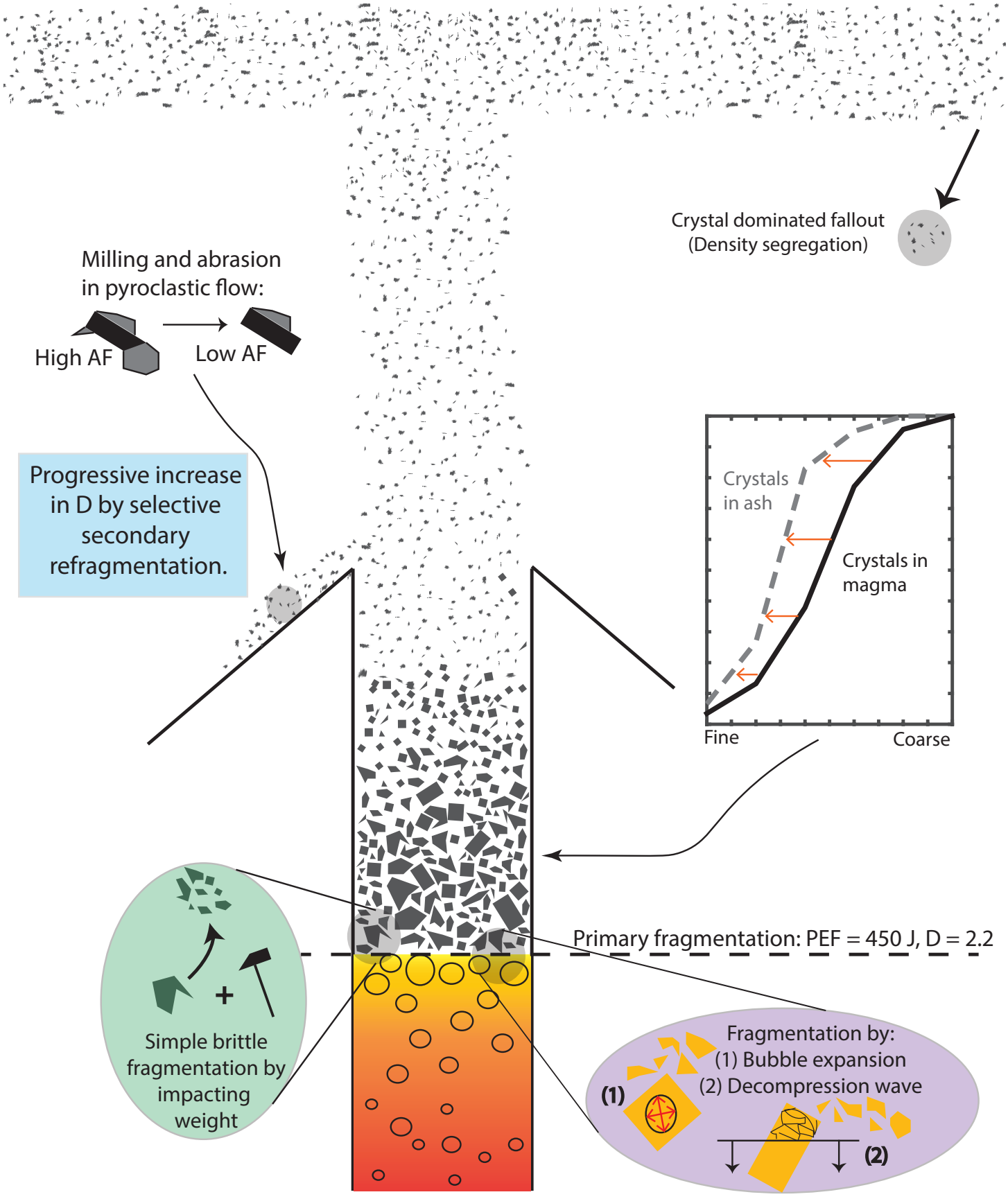

Figure 11: Jones et al (2016, JVGR)
Size: Single collumn

Supplementary Material (Fig s1)

Click here to download Electronic Supplementary Material (online publication only): Figure_S1.pdf

Supplementary Material (Fig s2)

Click here to download Electronic Supplementary Material (online publication only): Figure_S2.pdf